

FAINT SUBMILLIMETER GALAXY COUNTS AT 450 μm

CHIAN-CHOU CHEN¹, LENNOX L. COWIE¹, AMY J. BARGER^{1,2,3}, CAITLIN M. CASEY^{1,5}, NICHOLAS LEE¹,
DAVID B. SANDERS¹, WEI-HAO WANG⁴, AND JONATHAN P. WILLIAMS¹

¹ Institute for Astronomy, University of Hawaii, 2680 Woodlawn Drive, Honolulu, HI 96822, USA

² Department of Astronomy, University of Wisconsin-Madison, 475 North Charter Street, Madison, WI 53706, USA

³ Department of Physics and Astronomy, University of Hawaii, 2505 Correa Road, Honolulu, HI 96822, USA

⁴ Academia Sinica Institute of Astronomy and Astrophysics, P.O. Box 23-141, Taipei 10617, Taiwan

Received 2012 September 16; accepted 2012 November 13; published 2012 December 18

ABSTRACT

We present the results of SCUBA-2 observations at 450 μm and 850 μm of the field lensed by the massive cluster A370. With a total survey area >100 arcmin² and 1σ sensitivities of 3.92 and 0.82 mJy beam⁻¹ at 450 and 850 μm , respectively, we find a secure sample of 20 sources at 450 μm and 26 sources at 850 μm with a signal-to-noise ratio (S/N) >4 . Using the latest lensing model of A370 and Monte Carlo simulations, we derive the number counts at both wavelengths. The 450 μm number counts probe a factor of four deeper than the counts recently obtained from the *Herschel Space Telescope* at similar wavelengths, and we estimate that $\sim 47\%$ – 61% of the 450 μm extragalactic background light resolved into individual sources with 450 μm fluxes greater than 4.5 mJy. The faint 450 μm sources in the 4σ sample have positional accuracies of 3 arcsec, while brighter sources (S/N $>6\sigma$) are good to 1.4 arcsec. Using a deep radio map ($1\sigma \sim 6 \mu\text{Jy}$) we find that the percentage of submillimeter sources having secure radio counterparts is 85% for 450 μm sources with intrinsic fluxes >6 mJy and 67% for 850 μm sources with intrinsic fluxes >4 mJy. We also find that 67% of the $>4\sigma$ 450 μm sources are detected at 850 μm , while the recovery rate at 450 μm of $>4\sigma$ 850 μm sources is 54%. Combined with the source redshifts estimated using millimetric flux ratios, the recovered rate is consistent with the scenario where both 450 μm and 20 cm emission preferentially select lower redshift dusty sources, while 850 μm emission traces a higher fraction of dusty sources at higher redshifts. We identify potential counterparts in various wavelengths from X-ray to mid-infrared and measure the multiwavelength photometry, which we then use to analyze the characteristics of the sources. We find three X-ray counterparts to our robust submillimeter sample (S/N >5), giving an active galactic nucleus fraction for our 450 (850) μm sample of 3/8 (3/9) or 38% (33%). We also find a correlation between the K_s band and the 850 μm /20 cm flux ratio.

Key words: cosmology: observations – galaxies: formation – galaxies: starburst – gravitational lensing: strong – submillimeter: diffuse background – submillimeter: galaxies

Online-only material: color figures

1. INTRODUCTION

Based on studies of the integrated light originating from outside the Milky Way galaxy—the extragalactic background light (EBL)—we now know that there is a comparable amount of light absorbed by dust and re-radiated in the far-infrared (FIR)/submillimeter ($100 \mu\text{m} < \lambda < 1000 \mu\text{m}$) as there is seen directly in the optical/UV (Puget et al. 1996; Fixsen et al. 1998; Dole et al. 2006), which indicates that much of the star formation and active galactic nucleus (AGN) activity in the universe is hidden by dust. Understanding dusty star formation is therefore critical to a full understanding of galaxy formation.

The first step in such work is identifying the individual dusty galaxies. Observations have been made toward this goal using both the small space-based *Herschel Space Observatory* (hereafter *Herschel*; Pilbratt et al. 2010) and, at longer wavelengths, ground-based telescopes (e.g., the James Clerk Maxwell Telescope (JCMT)). However, the fraction of sources that can be identified with such observations has a fundamental limit due to the poor resolution. This limit is known as the confusion limit (Scheuer 1957; Condon 1974; Hogg 2001), which is the maximum sensitivity an observation is able to reach for a given beam size due to the overlap of sources on the map. Recent observations carried out by *Herschel* at 250, 350, and 500 μm

can only resolve a small amount of the EBL (15%, 10%, and 6%; Oliver et al. 2010) due to the confusion limit. With a 15 m dish, the JCMT blank-field submillimeter surveys with SCUBA (Holland et al. 1999) only resolved $\sim 20\%$ – 30% of the 850 μm EBL into distinct, bright submillimeter galaxies (SMGs) with $S_{850 \mu\text{m}} > 2$ mJy (e.g., Barger et al. 1998, 1999a; Hughes et al. 1998; Eales et al. 1999; Coppin et al. 2006) before reaching the confusion limit. The most recent surveys using LABOCA (Siringo et al. 2009) on the APEX telescope at 870 μm obtained similar results (Weiß et al. 2009).

The most fundamental consequence of the confusion limit is that the poor resolution at 850 μm prevents the study of faint SMGs below 2 mJy in blank fields. A small number of fainter SMGs with intrinsic fluxes between 0.1 and 2 mJy have been detected from observations of the fields of massive lensing clusters. In these fields, the intrinsically faint fluxes of background sources are gravitationally amplified to a detectable level. The sources found in this way contribute more than 50% of the 850 μm EBL (Smail et al. 1997, 2002; Cowie et al. 2002; Knudsen et al. 2008). However, the positional uncertainties of the 850 μm sources can cause large uncertainties in the amplifications and in the intrinsic source fluxes (Chen et al. 2011). It is therefore essential to conduct surveys on lensing cluster fields with as high a spatial resolution as possible to circumvent the confusion limit and to construct the most accurate possible number counts distribution.

⁵ Hubble Fellow.

The poor resolution (e.g., $14''$ FWHM on the JCMT at $850\ \mu\text{m}$) also makes identifying the counterparts in other wavelengths difficult and time consuming. Deep, high-resolution radio, mid-infrared (MIR), optical, UV, and X-ray observations have been used to identify candidate counterparts to the SMGs and to trace their star formation and AGN activity (Barger et al. 2000; Chapman et al. 2005; Pope et al. 2006; Ivison et al. 2007; Georgantopoulos et al. 2011). However, direct high-resolution submillimeter interferometric observations have shown that due to their clustered nature (Weiß et al. 2009), SMGs are likely to be resolved into multiple sources and that different tracers identify different counterparts based on their own biases (e.g., Wang et al. 2011; Barger et al. 2012; Smolčić et al. 2012; Karim et al. 2012).

Many of these problems can be avoided by observing at $450\ \mu\text{m}$ rather than at $850\ \mu\text{m}$. The higher spatial resolution at $450\ \mu\text{m}$ means that we can detect several times more sources before hitting the confusion limit, and the more accurate positions allow us to better determine the amplifications when observing lensed sources. In addition, while $850\ \mu\text{m}$ observations have the unique advantage of tracing the star-forming galaxies to very high redshifts ($z \sim 10$), thanks to the negative K -correction (Blain et al. 2002), it has been argued that owing to the location on the Rayleigh–Jeans tail of the blackbody spectral energy distribution (SED), the $850\ \mu\text{m}$ selection is biased against high dust temperature sources (Blain et al. 2004; Chapman et al. 2004; Casey et al. 2009). To mitigate this selection effect, observations at rest-frame wavelengths close to the peak of the blackbody SED ($\sim 100\text{--}200\ \mu\text{m}$) that are less affected by the dust temperature are needed. The SPIRE instrument mounted on *Herschel* is designed to do this job; however, its ability to detect sources is again heavily restricted by the confusion limit due to the small aperture size of the telescope.

$450\ \mu\text{m}$ mapping was very inefficient with SCUBA (Chapman et al. 2002; Smail et al. 2002). Based on a handful of extracted sources (<10) with $450\ \mu\text{m}$ fluxes above $10\ \text{mJy}$, only 15% of the $450\ \mu\text{m}$ EBL was resolved (Smail et al. 2002). The advent of SCUBA-2 (Holland et al. 2006) on the JCMT with its two orders of magnitude more pixels/bolometers than on SCUBA greatly boosts our ability to resolve the bulk of the $450\ \mu\text{m}$ EBL and to detect galaxies not biased by dust temperature. SCUBA-2 observes simultaneously at 450 and $850\ \mu\text{m}$ via a dichroic beam splitter. Unlike SCUBA, the bolometers on SCUBA-2 are optimized for observing at 450 and $850\ \mu\text{m}$, and the filter transmission, especially at $450\ \mu\text{m}$, is much better than that of SCUBA. Moreover, the field of view of SCUBA-2 is more than 10 times larger than that of SCUBA. With all of these new features, SCUBA-2 is an order of magnitude faster than SCUBA, which makes it possible to finally study the $450\ \mu\text{m}$ population in detail. The amount of FIR EBL that can be resolved by SCUBA-2 is unprecedented as we show later in the paper, and demonstrates both the power of SCUBA-2 and also the promise of the next generation of submillimeter telescopes (CCAT).

Here we describe the results that we have obtained on the lensing cluster field Abell 370 (A370) from our ongoing SCUBA-2 program to survey a sample of massive galaxy clusters at $450\ \mu\text{m}$. The goals of this program are to resolve the $450\ \mu\text{m}$ EBL as fully as possible, to efficiently identify the counterparts of the $850\ \mu\text{m}$ sources, and, most important of all, to study the nature of the SMG population in an unbiased fashion as possible. In Section 2, we discuss our SCUBA-2 observations, data reduction, and ancillary data. Since the

results involve a relatively new instrument, we describe the methodology in detail. Readers who are primarily interested in the results can skip directly to Section 3, where we describe our source extraction and present our catalog. In Section 4, we determine the number counts and the amount of the EBL that our data resolve at both 450 and $850\ \mu\text{m}$. In Section 5, we discuss the properties of the sources at submillimeter and radio wavelengths. Using the rich set of ancillary data on this field from the radio to the X-ray, in Section 6, we analyze the properties of the counterparts to the submillimeter sources, construct color–color and color–flux diagrams, and examine the nature of both 450 and $850\ \mu\text{m}$ sources. Finally, we summarize our results in Section 7. Throughout the paper, we adopt the AB magnitude system for the photometry. We also assume the Wilkinson Microwave Anisotropy Probe cosmology of $H_0 = 70.5\ \text{km s}^{-1}\ \text{Mpc}^{-1}$, $\Omega_M = 0.27$, and $\Omega_\Lambda = 0.73$ (Larson et al. 2011).

2. OBSERVATIONS, DATA REDUCTION, AND ANCILLARY DATA

We carried out the SCUBA-2 observations in 2011 December and in 2012 February and March (program IDs: M11BH26A and M12AH26A) under the best weather conditions (band 1, $\tau_{225\text{GHz}} < 0.05$). A370 has a large Einstein ring with an angular diameter size of $3'$. To exploit the strong magnification and to efficiently use any available time to discover faint sources, we adopted the CV Daisy pattern⁶ to perform the observations. This observing mode is optimal for an area less than $4'$. Each scan/cycle takes around 20 minutes to complete. Flat fields were taken at the beginning and end of each scan, however, only the first one is used for data reduction. The extinction correction coefficients are obtained from the JCMT water vapor radiometer using the 183 GHz water line to calculate the precipitable water vapor along the line of sight of the telescope (Dempsey et al. 2012).

We reduced the data using the Dynamic Iterative Map-Maker (DIMM) in the SMURF package from the STARLINK software developed by the Joint Astronomy Centre (Jenness et al. 2011) released before 2012 July 1. The program automatically performs dark subtraction, flat fielding, extinction corrections, and data flagging. It also removes the DC steps from each bolometer, performs frequency domain filtering, and concatenates the reduced data from each chip to produce the final sky map. DIMM provides considerable freedom to the user to fine-tune the parameters that control the jobs mentioned above, and those parameters are stored in a configuration file that is included in DIMM during the data reduction.

There are four detector chips in each waveband with 1280 (40×32) bolometers per chip. We ran DIMM on the individual chips in each scan and used the MOSAIC_JCMT_IMAGES recipe in Pipeline for Combining and Analyzing Reduced Data (PICARD; Jenness et al. 2008) to mosaic and co-add the maps. We found this method produces better signal-to-noise (S/N) maps than running DIMM on all the data at once. The noise maps and the exposure time maps were also created from DIMM. The noise map is obtained by computing the variance of the data that lands in each pixel. We tested the robustness of the noise map created from DIMM by checking the standard deviation of the S/N maps. If the noise map is robust, then the standard deviation

⁶ A detailed description of the CV Daisy pattern can be found at http://www.jach.hawaii.edu/JCMT/continuum/scuba2/scuba2_obsmodes.html#scan.

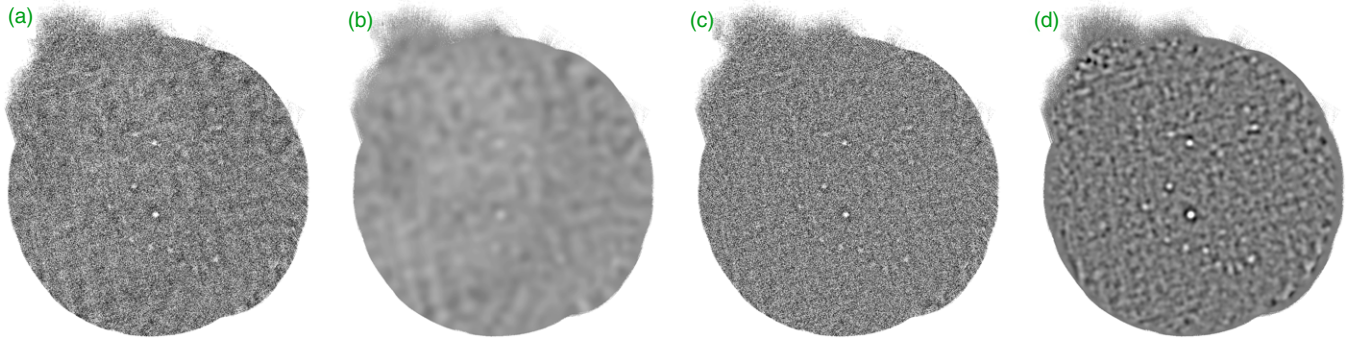


Figure 1. Demonstration of 850 μm maps for post-processing. (a) Map created from DIMM. (b) Map in (a) convolved with a broad Gaussian (FWHM = 30'' for 850 μm). (c) Map in (a) subtracted from map in (b). (d) Result of performing matched-filter on map in (c). Note that these are all S/N maps scaled to maximize the visibility of the sources.

(A color version of this figure is available in the online journal.)

of the S/N map should be close to 1. All the noise maps are accurate with an underestimation less than 5%. We suspect that the cause of the small underestimation is the correlated noise from the large-scale structure caused by the atmospheric noise (see Figure 1(a)), which is ultimately subtracted out in our post-processing technique (Section 2.1).

2.1. Flux Calibration

We adopted the configuration file *dimconfig_bright_compact.lis* provided by SMURF for DIMM to produce the calibrators' maps in units of picowatts (pW), and we used the CALC_SCUBA2_FCF recipe from PICARD to calculate the flux conversion factors (FCFs) for the SCUBA-2 maps.

The recipe performs a Gaussian fit for the calibrator and computes the total flux in units of pW arcsec². It then divides the expected flux in Jy by the computed flux to obtain the FCF_[ARCSEC] in units of Jy pW⁻¹ arcsec⁻². It has been reported that FCF_[ARCSEC] is very stable from extensive examination of the calibrators observed over the period of SCUBA-2 commissioning and science verification (Dempsey et al. 2012). We doubled checked this on our own calibrators and confirmed that the number is indeed stable.

The majority of SMGs are found to be located at high redshifts ($z > 1$), with the median $z \sim 2.5$ (Chapman et al. 2005; Wardlow et al. 2011). Based on high-resolution interferometric observations, a physical resolution less than a few kpc is needed to resolve individual SMGs (Knudsen et al. 2010). With our 7".5 resolution at 450 μm , we can barely resolve sources at $z \sim 0.1$. Thus, it is safe to assume that SMGs are mostly unresolved point sources at the resolution of our maps.

To optimize the point-source extraction, we adopted the matched-filter algorithm, which is a maximum likelihood estimator of the source strength, for post-processing in order to increase the S/N for point-source detection (e.g., Serjeant et al. 2003). Assuming $S(i, j)$ and $\sigma(i, j)$ are the signal and rms noise maps produced by DIMM and $\text{PSF}(i, j)$ is the signal point-spread function, the filtered signal map $F(i, j)$ would be

$$F(i, j) = \frac{\sum_{i,j} [S(i, j)/\sigma(i, j)^2 \times \text{PSF}(i, j)]}{\sum_{i,j} [1/\sigma(i, j)^2 \times \text{PSF}(i, j)^2]}, \quad (1)$$

and the filtered noise map $N(i, j)$ would be

$$N(i, j) = \frac{1}{\sqrt{\sum_{i,j} [1/\sigma(i, j)^2 \times \text{PSF}(i, j)^2]}}. \quad (2)$$

Ideally, the PSF for the matched-filter algorithm is a Gaussian normalized to a peak of unity with FWHM equal to the JCMT beam size at a given wavelength (i.e., 7".5 at 450 μm and 14'' at 850 μm). However, the map produced from DIMM usually has low spatial frequency structures that need to be subtracted off before performing the source extraction. Thus, before running matched-filter, we convolved the map with a broad Gaussian (22'' at both 450 and 850 μm) normalized to a sum of unity and subtracted this convolved map from the original map. Note that we experimented with different FWHM sizes of the broad Gaussian used to convolve the maps for background subtraction, and we found that the source fluxes and the S/N are not sensitive to the size of the FWHM (with variations lower than 5%) for reasonable choices. We adopted 22'', which gives a good suppression of the negative signals. In Figure 1, we show the before and after versions of the background subtraction and matched-filter. To determine the fluxes, we processed the PSF used for matched-filter similarly. It becomes a Gaussian with a convolved broader Gaussian subtracted off, which gives a Mexican hat-like wavelet. We adopted the PICARD recipe SCUBA2_MATCHED_FILTER for the tasks described above.

Because of the atmospheric fluctuation, especially at 450 μm , the signal distribution is not always a perfect Gaussian with the expected FWHM, which could lead to incorrect flux measurements if we adopt the standard PSF for the matched-filter. However, this uncertainty can be taken into account by going through the same source extraction process on the calibrators as was done on the science maps. We therefore applied matched-filter to the calibrators with the same PSF function used on the science maps, including the background subtraction, and divided the calibrators' expected flux by the after-matched-filter fitted peak flux to obtain FCF_[BEAMMATCH] in units of Jy beam⁻¹ pW⁻¹. This is the FCF that we used to calibrate our science maps.

There are several calibrators available each night, and the variation of FCF_[BEAMMATCH] between calibrators is usually larger than the statistical error. We chose the primary calibrator Uranus most of the time because of its high S/N. Moreover, compared to the other primary calibrator Mars, the angular size of Uranus is more stable and smaller than the beam size (unresolved), which is ideal for flux calibration for point sources. However, in cases where the phase of Uranus is highly distorted, we considered the secondary calibrator. Table 1 shows the two-dimensional Gaussian fitted FWHM on the x and y axes, along with the FCF_[BEAMMATCH] of all our calibrators. The FWHM of the PSFs and the FCFs are very stable for all our observations (less than 10% variations),

Table 1
FWHM of the PSFs and FCFs of the Calibrators

Date	Calibrators	FWHM _x (arcsec; 450/850)	FWHM _y (arcsec; 450/850)	FCF_[BEAMMATCH] (Jy beam ⁻¹ pW ⁻¹ ; 450/850)
122611	CRL618	8.96/13.26	8.64/13.03	831.513/606.928
122811	Uranus	8.74/13.06	8.41/13.23	750.590/567.313
	Uranus	9.41/13.40	9.51/13.94	819.377/602.322
020412	Uranus	8.32/12.77	9.44/13.65	697.301/568.398
020512	Uranus	8.47/13.06	8.71/13.45	710.364/563.341
Average		8.78/13.11	8.94/13.46	761.829/581.660
Stddev		0.43/0.24	0.50/0.36	61.454/21.111

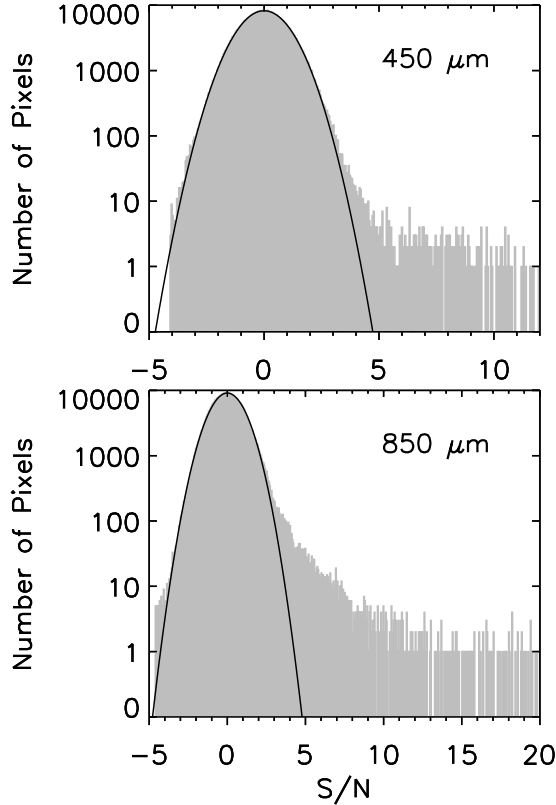


Figure 2. Histograms of the S/N values of the pixels located within the regions where the noise level is less than three times the central rms (gray area). The black curves represent the region of noise. The excess negative signals at 850 μm come from one negative source (see discussion in Section 3.3).

which is evidence that the PSFs at both wavelengths are well determined.

2.2. Science Maps

We adopted the configuration file *dimconfig_blank_field.lis* for our science maps. The biggest difference between *dimconfig_blank_field.lis* and *dimconfig_bright_compact.lis* used for calibrators is that the latter is less aggressive in identifying bad bolometers and DC steps, in order to ease the misidentification between bad bolometers/DC steps and bright sources.

For each night of data, we used DIMM to reduce the data on the individual chips in each scan and then co-added them to produce one science map and one calibrator map. We performed the matched-filter algorithm on both maps and applied the FCF_[BEAMMATCH] obtained from the calibrator to the science map. Finally, we co-added all the science maps

Table 2
SCUBA-2 Observations on A370 Field

R.A. (J2000; h:m:s)	02:39:53
Decl. (J2000; °:':")	-01:34:38
Area (850 μm ; arcmin ²) ^a	124.579
Area (450 μm ; arcmin ²) ^a	121.095
Central noise (850 μm ; 1 σ ; mJy beam ⁻¹)	0.82
Central noise (450 μm ; 1 σ ; mJy beam ⁻¹)	3.92

Notes. ^a Total area to three times the central noise level.

that were created on a night-by-night basis to produce the final map for source extraction.

Because we subtracted the original signal map from a self-convolved map during the post-processing to get rid of the large-scale structure, negative troughs are generated around strong sources (see Figure 1(d)). Those negative troughs may suppress nearby weak sources. We therefore re-did the post-processing by masking out sources with S/N greater than 4 and iterated this procedure until there were no new sources with S/N greater than 4. We then put the masked sources back into the masked images to generate a hybrid map, which is the final map that we used for our analysis.

The noise map created through Equation (2) would inevitably underestimate the noise level because of the spatially correlated noise (Figure 1(d)). We corrected for this underestimation by multiplying the noise map by the standard deviation of the original S/N map (Equation (1) divided by Equation (2)). In Figure 2, we plot the histograms of the final data maps at both wavelengths within the effective regions. The effective regions are the regions where the noise level is less than three times the central rms, meaning the region where the effective exposure time is more than one-ninth of the central exposure time. The black curves represent the region of noise. The excess negative signals at 850 μm come from one negative source (see discussion in Section 3.3). We present the final central noise level, along with other observational information on A370, in Table 2.

2.3. Astrometry Calibration

SMGs are often traced by 20 cm sources, thanks to the tight and universal FIR–radio flux correlation (Helou et al. 1985; Condon 1992). Although this correlation must break down at very high redshifts due to the Compton cooling between the relativistic electrons and the cosmic microwave background photons, so far no clear evidence for evolution of this correlation has been seen to $z \sim 5$ (Barger et al. 2012).

Since most SMGs found so far are located at $z < 5$, the radio sources detected in high-resolution maps taken by interferometers are a good sample to use for our absolute astrometry

Table 3
A370 Optical, NIR, MIR, FIR, Radio Photometry

Wavebands	Instruments/Telescopes	References
X-ray (2–7 keV)	ACIS-S3/ <i>Chandra</i>	Barger et al. (2001)
X-ray (0.5–2 keV)	ACIS-S3/ <i>Chandra</i>	Barger et al. (2001)
z	Suprime-Cam/Subaru	Hu et al. (2010)
J	ULBCam/UH2.2m	Keenan et al. (2010)
H	ULBCam/UH2.2m	Keenan et al. (2010)
K_s	WFCAM/UKIRT	Keenan et al. (2010)
3.6 μm	IRAC/ <i>Spitzer</i>	PID: 60034
4.5 μm	IRAC/ <i>Spitzer</i>	PID: 60034
5.8 μm	IRAC/ <i>Spitzer</i>	PID: 137
8.0 μm	IRAC/ <i>Spitzer</i>	PID: 137
450/850 μm	SCUBA-2/JCMT	This work
20 cm	VLA	Wold et al. (2012)

calibration. We searched for the offset of the submillimeter maps that maximized the stacked submillimeter signal over all the radio sources in the Wold et al. (2012) radio catalog of the field. We found a systematic shift of ($0''$, $2''$) in our 850 μm map and ($-1''$, $1''$) in our 450 μm map. We corrected this small offset before proceeding to the source extraction.

2.4. Ancillary Data

A370 is one of the most extensively studied gravitational lensing cluster fields, with its multiwavelength observations from the X-ray to the radio. In Table 3, we list all the data on A370 that we used in this paper, along with the corresponding references.

The *Chandra* X-ray survey of the A370 field with 66.6 ks of useful exposure time has a 1σ sensitivity of $\sim 10^{-15}$ erg $\text{cm}^2 \text{s}^{-1}$ in the 2–7 keV band and $\sim 3 \times 10^{-16}$ erg $\text{cm}^2 \text{s}^{-1}$ in the 0.5–2 keV band (Bautz et al. 2000; Barger et al. 2001).

The optical z -band data were taken by Hu et al. (2010) using Suprime-Cam on Subaru for a study of high-redshift Ly α emitters. The 5σ sensitivity for a $3''$ diameter aperture is 25.4 AB magnitude.

The deep NIR J , H , K_s observations were carried out by Keenan et al. (2010) using ULBCam on the University of Hawaii 2.2 m (UH2.2m) and WFCam on UKIRT. The 5σ detection limits are 23.5, 23.0, and 23.0 AB magnitude, respectively. We adopted their configuration files and used SExtractor (Bertin & Arnouts 1996) to extract sources.

The A370 field was first surveyed by *Spitzer* (Werner et al. 2004) in 2006 (PI: Giovanni Fazio; PID: 137) in all the IR Array Camera (IRAC; Fazio et al. 2004) bands (3.6–8.0 μm). Data with wider coverage at 3.6 and 4.5 μm were later taken in 2009 and 2010 (PI: Eiichi Egami; PID: 60034) when *Spitzer* entered the warm phase. We again used SExtractor to extract sources from the *Spitzer* maps. We measured the source fluxes using apertures with diameters of $4''.8$ for 3.6 μm and 4.5 μm and $6''.0$ for 5.8 μm and 8.0 μm , which are roughly three times the FWHM of the PSFs and are the same as those used in Wang et al. (2004). We estimated the sensitivities using Gaussian fits to the fluxes measured at random source-free positions, finding 5σ limits of 23.3 at 3.6 μm and 4.5 μm , 23.0 at 5.8 μm , and 22.6 at 8.0 μm , all in AB magnitudes.

The deep Very Large Array (VLA) radio data of the field were taken using both the A and B configurations. The final image reaches a 5σ limit of $28.5 \mu\text{Jy beam}^{-1}$ near the central region with a beam size of $\sim 1''.7$ (Wold et al. 2012).

3. SOURCE IDENTIFICATION AND CATALOG

3.1. Source Extraction

On both maps, we first extracted sources that have a peak S/N greater than 3.0 within the effective regions. The way we extracted the source is that we found the maximum pixel within the desired region, took the position and the value information of the peak, and subtracted a PSF centered at the source and scaled accordingly. We iterated this process until the peak S/N value was less than 3.0. We treated these peaks as the preliminary catalogs at 450 μm and 850 μm . We then cross-correlated the two catalogs to find the counterparts in the other bandpass. We considered a counterpart recovered if the position of the 450 μm source lay within the 850 μm beam. The only exception was A370-450.9, which lies slightly outside the beam area of A370-850.5 but likely contributes a certain amount of the 850 μm flux and makes A370-850.5 appear elongated. We considered both A370-450.9 and A370-450.11 to be counterparts to A370-850.5.

To form the final catalogs, we kept every $>4\sigma$ source in the preliminary catalogs, as well as every $>3\sigma$ source that had a $>3\sigma$ counterpart in the other bandpass. In Table 4 (Table 5), we give the $>4\sigma$ 450 (850) μm sources, as well as the $>3\sigma$ 450 (850) μm sources with $>3\sigma$ 850 (450) μm counterparts. In Column 1, we give the name of the source; in Column 2, our identification for the source; in Columns 3 and 4, the right ascension and declination in J2000 coordinates; in Column 5, the S/N in the discovery bandpass; in Column 6, the flux in the discovery bandpass; in Column 7, our identification for the counterpart in the other bandpass, where available; in Column 8, the S/N for that counterpart or the S/N measured at the peak position in the other bandpass; in Column 9, the flux for that counterpart or the flux measured at the peak position in the other bandpass.

We give our assessment of the reliability of our source extraction in Section 3.2. We show our final S/N images in Figure 3 overplotted with all the sources in Tables 4 and 5 (red circles and blue squares for 850 μm and 450 μm , respectively) and with the noise contours. In total, we detected 26 sources at 850 μm and 20 sources at 450 μm . The number density is 3 (10) sources per 1000 beam areas at 450 (850) μm , which indicates that our maps are not yet reaching the confusion limit (roughly 1 source per 30 beam areas). Thus, the flux boosting and the positional errors caused by source confusion should be negligible (Hogg 2001). Note that the maps are all gridded into $1''$ by $1''$ pixels. We experimented with different pixel sizes and found that the results are not affected by the different choices. This is because the matched-filter technique is not affected by the pixel size (Equations (1) and (2)), as long as the PSF is well sampled.

3.2. Reliability of Source Extraction

We used two methods to quantify the number of spurious sources above 4σ that might be included in our catalogs. First, we created a map with the same spatial dimensions as the real maps, populated the pixels with random Gaussian signal convolved with the PSF at the given wavelength, and then ran the peak identification. We iterated this process 100 times at each wavelength and found that we should expect 1.8 ± 1.3 sources at 450 μm and 0.6 ± 0.8 sources at 850 μm to be spurious.

Second, we performed our same source extraction method on the inverted maps, where the negative signal becomes positive and vice versa, to see how many negative sources are present at

Table 4
SCUBA-2 450 μm Detected Sources

Name	ID	R.A. (J2000)	Decl. (J2000)	S/N	f_{450} (mJy)	Counterpart ID ₈₅₀	$S/N_{c,850}$ (mJy)	$f_{c,850}$
(1)	(2)	(3)	(4)	(5)	(6)	(7)	(8)	(9)
>4σ sample								
SMM J023951.8–013558	A370-450.1	2 39 51.83	–1 35 58.0	11.97	54.40 \pm 4.54	A370-850.1	20.48	20.40 \pm 1.00
SMM J023956.5–013426	A370-450.2	2 39 56.50	–1 34 26.0	10.93	45.81 \pm 4.19	A370-850.3	9.16	7.89 \pm 0.86
SMM J023952.1–013208	A370-450.3	2 39 52.10	–1 32 08.0	8.79	46.63 \pm 5.31	A370-850.2	11.68	11.93 \pm 1.02
SMM J023945.6–013244	A370-450.4	2 39 45.63	–1 32 44.0	5.18	31.17 \pm 6.02	A370-850.18	4.18	4.96 \pm 1.19
SMM J023948.6–013752	A370-450.5	2 39 48.56	–1 37 52.0	4.76	26.09 \pm 5.48	A370-850.6	7.35	8.45 \pm 1.15
SMM J023935.2–013614	A370-450.6	2 39 35.23	–1 36 14.0	4.69	33.48 \pm 7.13	...	–1.04	–1.48 \pm 1.43
SMM J023953.0–013746	A370-450.7	2 39 52.97	–1 37 46.0	4.59	26.29 \pm 5.73	A370-850.8	6.06	6.98 \pm 1.15
SMM J023947.0–013331	A370-450.8	2 39 46.96	–1 33 31.0	4.50	21.21 \pm 4.72	...	2.43	2.38 \pm 0.98
SMM J023938.5–013815	A370-450.9	2 39 38.49	–1 38 15.0	4.46	29.30 \pm 6.57	A370-850.5	7.43	11.13 \pm 1.50
SMM J023958.1–013424	A370-450.10	2 39 58.10	–1 34 24.0	4.38	19.45 \pm 4.44	...	1.62	1.48 \pm 0.91
SMM J023938.7–013827	A370-450.11	2 39 38.69	–1 38 27.0	4.05	26.73 \pm 6.60	A370-850.5	7.43	11.13 \pm 1.50
SMM J023940.2–013345	A370-450.12	2 39 40.16	–1 33 45.0	4.03	21.98 \pm 5.46	...	1.90	2.17 \pm 1.14
>3σ sample with >3σ counterparts at 850 μm								
SMM J024005.2–013629	A370-450.13	2 40 05.17	–1 36 29.0	3.79	21.82 \pm 5.75	A370-850.26	3.07	4.27 \pm 1.39
SMM J023957.6–013457	A370-450.14	2 39 57.64	–1 34 57.0	3.77	16.80 \pm 4.46	A370-850.17	4.21	3.77 \pm 0.90
SMM J023946.0–013837	A370-450.15	2 39 46.03	–1 38 37.0	3.75	22.88 \pm 6.10	A370-850.9	5.74	7.42 \pm 1.29
SMM J023956.2–013139	A370-450.16	2 39 56.23	–1 31 39.0	3.67	19.25 \pm 5.24	A370-850.10	5.58	6.05 \pm 1.08
SMM J023938.2–013117	A370-450.17	2 39 38.16	–1 31 17.0	3.41	28.24 \pm 8.27	A370-850.4	7.48	11.79 \pm 1.58
SMM J024001.7–013531	A370-450.18	2 40 01.70	–1 35 31.0	3.19	16.24 \pm 5.09	A370-850.7	6.96	7.61 \pm 1.09
SMM J023940.5–013721	A370-450.19	2 39 40.50	–1 37 21.0	3.15	20.74 \pm 6.59	A370-850.25	3.88	5.28 \pm 1.36
SMM J023937.8–013310	A370-450.20	2 39 37.83	–1 33 10.0	3.12	18.94 \pm 6.08	A370-850.15	4.08	5.14 \pm 1.26

Table 5
SCUBA-2 850 μm Detected Sources

Name	ID	R.A. (J2000)	Decl. (J2000)	S/N	f_{850} (mJy)	Counterpart ID ₄₅₀	$S/N_{c,450}$ (mJy)	$f_{c,450}$
(1)	(2)	(3)	(4)	(5)	(6)	(7)	(8)	(9)
>4σ sample								
SMM J023952.0–013559	A370-850.1	2 39 51.97	–1 35 59.0	20.48	20.40 \pm 1.00	A370-450.1	11.97	54.40 \pm 4.54
SMM J023952.2–013208	A370-850.2	2 39 52.17	–1 32 08.0	11.68	11.93 \pm 1.02	A370-450.3	8.79	46.63 \pm 5.31
SMM J023956.6–013428	A370-850.3	2 39 56.57	–1 34 28.0	9.16	7.89 \pm 0.86	A370-450.2	10.93	45.81 \pm 4.19
SMM J023938.2–013119	A370-850.4	2 39 38.23	–1 31 19.0	7.48	11.79 \pm 1.58	A370-450.17	3.41	28.24 \pm 8.27
SMM J023939.0–013823	A370-850.5	2 39 38.96	–1 38 23.0	7.43	11.13 \pm 1.50	A370-450.11	4.05	26.73 \pm 6.60
						A370-450.9	4.46	29.30 \pm 6.57
SMM J023948.8–013754	A370-850.6	2 39 48.76	–1 37 54.0	7.35	8.45 \pm 1.15	A370-450.5	4.76	26.09 \pm 5.48
SMM J024001.8–013534	A370-850.7	2 40 01.84	–1 35 34.0	6.96	7.61 \pm 1.09	A370-450.18	3.19	16.24 \pm 5.09
SMM J023953.0–013745	A370-850.8	2 39 53.03	–1 37 45.0	6.06	6.98 \pm 1.15	A370-450.7	4.59	26.29 \pm 5.73
SMM J023946.1–013839	A370-850.9	2 39 46.10	–1 38 39.0	5.74	7.42 \pm 1.29	A370-450.15	3.75	22.88 \pm 6.10
SMM J023956.2–013140	A370-850.10	2 39 56.17	–1 31 40.0	5.58	6.05 \pm 1.08	A370-450.16	3.67	19.25 \pm 5.24
SMM J024003.0–013117	A370-850.11	2 40 03.04	–1 31 17.0	5.27	6.98 \pm 1.33	...	2.14	12.41 \pm 5.79
SMM J023957.0–013721	A370-850.12	2 39 57.03	–1 37 21.0	5.26	6.79 \pm 1.29	...	2.03	14.03 \pm 6.91
SMM J023939.9–013021	A370-850.13	2 39 39.90	–1 30 21.0	5.18	8.43 \pm 1.63	...	0.26	2.31 \pm 8.83
SMM J023945.4–013731	A370-850.14	2 39 45.43	–1 37 31.0	4.72	5.72 \pm 1.21	...	1.05	6.08 \pm 5.80
SMM J023938.0–013309	A370-850.15	2 39 38.03	–1 33 09.0	4.60	5.77 \pm 1.25	A370-450.20	3.12	18.94 \pm 6.08
SMM J023941.4–013848	A370-850.16	2 39 41.43	–1 38 48.0	4.33	6.40 \pm 1.48	...	1.95	12.81 \pm 6.58
SMM J023957.6–013455	A370-850.17	2 39 57.57	–1 34 55.0	4.21	3.77 \pm 0.90	A370-450.14	3.77	16.80 \pm 4.46
SMM J023945.6–013243	A370-850.18	2 39 45.56	–1 32 43.0	4.18	4.96 \pm 1.19	A370-450.4	5.18	31.17 \pm 6.02
SMM J023947.4–012920	A370-850.19	2 39 47.36	–1 29 20.0	4.13	6.89 \pm 1.67	...	1.77	15.52 \pm 8.78
SMM J024004.1–012851	A370-850.20	2 40 04.10	–1 28 51.0	4.10	8.32 \pm 2.03	...	0.22	3.39 \pm 15.37
SMM J024010.9–013635	A370-850.21	2 40 10.91	–1 36 35.0	4.04	6.93 \pm 1.72	...	–0.10	–0.76 \pm 7.64
SMM J024003.0–013051	A370-850.22	2 40 02.97	–1 30 51.0	4.03	5.22 \pm 1.30	...	0.57	3.40 \pm 5.93
SMM J023945.0–013654	A370-850.23	2 39 45.03	–1 36 54.0	4.02	5.21 \pm 1.30	...	1.59	9.52 \pm 6.00
SMM J023951.6–013035	A370-850.24	2 39 51.63	–1 30 35.0	4.00	4.64 \pm 1.16	...	1.33	8.38 \pm 6.28
>3σ sample with >3σ counterparts at 450 μm								
SMM J023940.6–013719	A370-850.25	2 39 40.56	–1 37 19.0	3.88	5.28 \pm 1.36	A370-450.19	3.15	20.74 \pm 6.59
SMM J024005.4–013633	A370-850.26	2 40 05.44	–1 36 33.0	3.07	4.27 \pm 1.39	A370-450.13	3.79	21.82 \pm 5.75

Table 6
SCUBA-2 850 μm Sources Compared with the Literature

Source ID	S_{850} (mJy)	Chen et al. S_{850} (mJy)	R.A. Offset ($''$)	Decl. Offset ($''$)	Cowie et al. S_{850} (mJy)	R.A. Offset ($''$)	Decl. Offset ($''$)	Smail et al. S_{850} (mJy)	R.A. Offset ($''$)	Decl. Offset ($''$)
A370-850.1	20.40 ± 1.00	21.06 ± 1.34	-1.0	0.0	23.0 ± 1.9	-1.0	0.0
A370-850.3	7.89 ± 0.86	7.95 ± 0.60	-0.3	-1.5	6.68 ± 0.58	0.9	-1.0	11.0 ± 1.9	-2.6	-1.0
A370-850.17	3.77 ± 0.90	3.49 ± 0.66	1.0	1.0

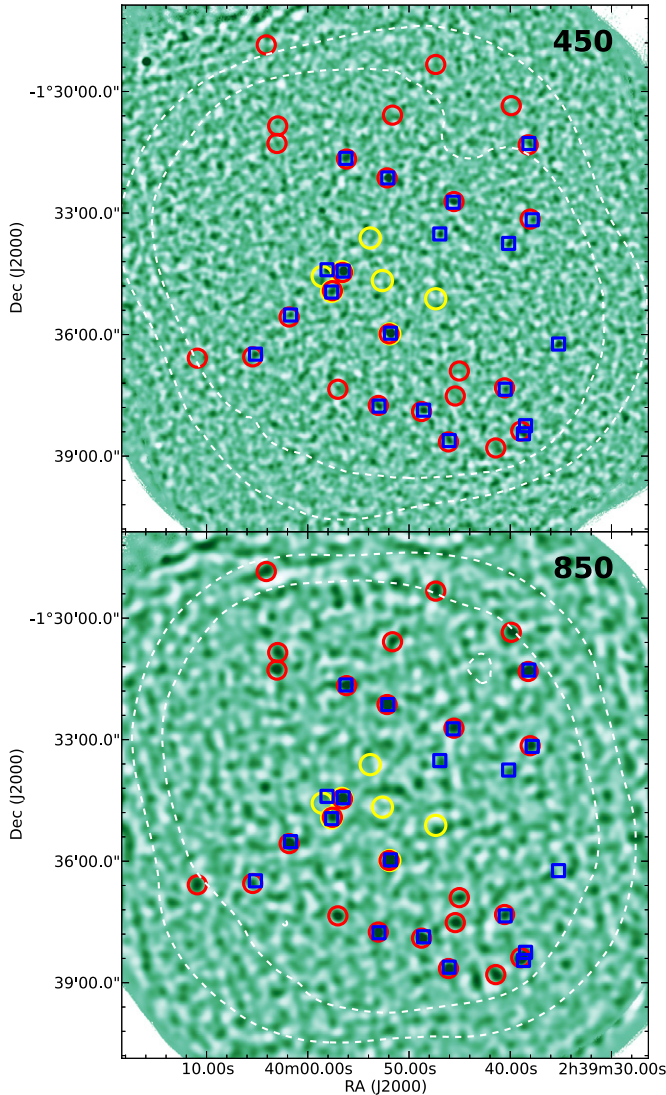


Figure 3. A370 SCUBA-2 S/N maps at 450 μm (top panel) and 850 μm (bottom panel) with a linear green scale from -4 to 4 . The size of both maps is $13' \times 13'$. Blue squares are the 20 450 μm sources given in Table 4, and red circles are the 26 850 μm sources given in Table 5. Yellow circles are SCUBA 850 μm sources from Cowie et al. (2002). White dashed curves are noise contours with levels $0.82 \times (2, 3)$ mJy beam $^{-1}$ at 850 μm and $3.92 \times (2, 3)$ mJy beam $^{-1}$ at 450 μm . The sizes of the circles and squares correspond to two times the beam FWHM of their respective wavelength (Table 1).

(A color version of this figure is available in the online journal.)

$>4\sigma$. We found 4 and 1 at 450 and 850 μm , respectively, which agrees reasonably well with our first approach and means that we could have that many spurious sources in our $>4\sigma$ catalogs.

For the 3σ sources identified as being present in both bandpasses, we again created random noise maps as described above, extracted sources between 3 and 4σ , and then cross-correlated them with the $>3\sigma$ sources extracted from the real maps at the other bandpass. We iterated this process 1000 times

Table 7
SCUBA-2 450 μm Sources Compared with the Literature

Source ID	S_{450} (mJy)	Smail et al. S_{450} (mJy)	R.A. Offset ($''$)	Decl. Offset ($''$)
A370-450.1	54.40 ± 4.54	85 ± 10	1.0	1.0
A370-450.2	45.81 ± 4.19	42 ± 10	-1.5	1.0

and found 0.2 and 0.3 spurious sources at 450 and 850 μm . In other words, sources identified at the 3σ level at both wavelengths are even more reliable than $>4\sigma$ sources only detected in one bandpass.

3.3. Comparison with Previous Catalogs

A370 was surveyed by SCUBA at both 450 and 850 μm within the circular region centered at the cluster centroid with a radius less than $1'5$ (Cowie et al. 2002; Smail et al. 2002). A370-850.3 was also observed (Chen et al. 2011) with the high-resolution Submillimeter Array (SMA; Ho et al. 2004). We list our detected sources within the SCUBA observed region along with previous results in Tables 6 and 7. Our maps do not recover all the sources detected in Cowie et al. (2002) because their maps have better sensitivity (<0.8 mJy beam $^{-1}$) at 850 μm . However, most of the recovered sources agree with the literature in terms of their fluxes and positions, except for the flux on A370-450.1 given by Smail et al. (2002). Knudsen et al. (2008) found that it is difficult to reliably calibrate the SCUBA 450 μm sources, because the PSF is not well described by a two-dimensional Gaussian and is very sensitive to the deformation of the JCMT dish. Thus, the 450 μm fluxes obtained from SCUBA could be problematic. This problem is significantly less in the SCUBA-2 maps, since, as we showed in Table 1, the PSFs at both 450 μm and 850 μm are stable and well modeled.

3.4. Completeness Tests

We took the noise maps created in the previous sections and ran a completeness test. We randomly populated the image with sources of a given flux and then ran the source extraction on the maps down to 4σ to see if we could recover the added sources. A source is considered recovered if it is detected above 4σ and if its position is within the beam area. We iterated this process 5000 times on each map with a flux step of 1 mJy (0.5 mJy) from 0.1 to 30.1 mJy for 450 (850) μm to estimate the completeness. We plot the results in Figure 4. The 50% completeness is around 4 and 17 mJy at 850 and 450 μm , respectively, and the 80% completeness is around 5 and 21 mJy, respectively.

4. NUMBER COUNTS

A370 is one of the most extensively studied gravitational lensing cluster fields with a well-constrained lensing model. We used LENSTOOL, a software package that models the effects of gravitational lensing by taking three-dimensional

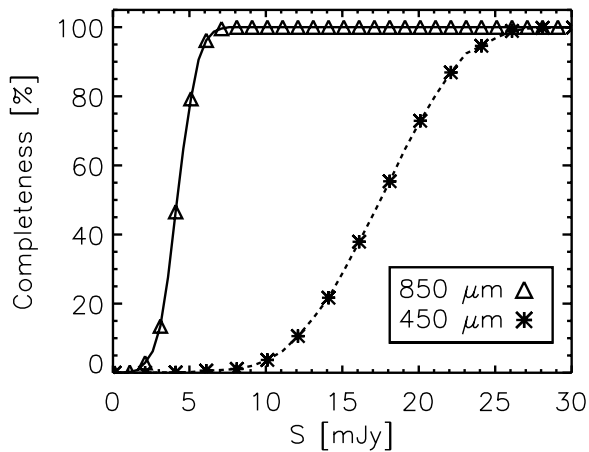


Figure 4. Result of the completeness tests on A370 at 450 μm (asterisks, dashed curve) and 850 μm (triangles, solid curve) vs. flux. In the simulation, the flux step at 450 (850) μm is 1 mJy (0.5 mJy). For a clear visual demonstration, the spacing between the asterisks is 2 mJy, and the spacing between the triangles is 1 mJy.

mass distributions within the cluster into account (Kneib et al. 1996), and adopted the latest lensing model from Richard et al. (2010) to compute the lensing magnification. We first derived raw number counts directly from the detected sources in our catalogs. We then estimated the true number counts and the errors on the raw number counts using Monte Carlo simulations. Finally, we calculated the amount of EBL resolved based on the final adopted true number counts curves. We discuss our procedure in more detail in the following subsections. Note that in order to undertake a simple and clear analysis, in this section we only used sources that were independently and uniformly selected at $>4\sigma$ in each bandpass without regard to whether there was a submillimeter counterpart in the other bandpass.

4.1. Delensed Raw Number Counts

The SCUBA-2 850 μm sources have a coarse resolution with a beam size of $14''$, which can cause large uncertainties in estimating the magnifications where the sources are strongly amplified (Chen et al. 2011). Thus, for 850 μm sources with a clear counterpart identified in either deep radio interferometric maps, 450 μm data, or submillimeter interferometric maps from the SMA (see Section 5), we adopted the redshifts and the positions of the counterparts for estimating the magnifications. The A370 cluster itself is at $z = 0.37$. For any sources having moderate amplifications with redshifts beyond $z = 1$, the amplification is only weakly dependent on the redshifts (Blain et al. 1999). Thus, for sources without redshift measurements, we adopt $z = 2.5$ based on the current finding that the median redshift of the SMG population is around 2.5 (Chapman et al. 2005; Wardlow et al. 2011).

Number counts are usually described in two ways: cumulative number counts or differential number counts. When the sample size is small, cumulative number counts give a cleaner visual picture of the underlying shape of the counts; however, errors on the cumulative counts are correlated and need to be carefully taken into account when one tries to fit the counts. On the other hand, differential counts have independent errors on each count measurement, making it straightforward to do χ^2 fitting on the counts. Our sample size is big enough with at least 10 sources in each bandpass that we can focus on analyzing the differential counts. In some cases we will also present the cumulative counts, but those are based on the differential counts.

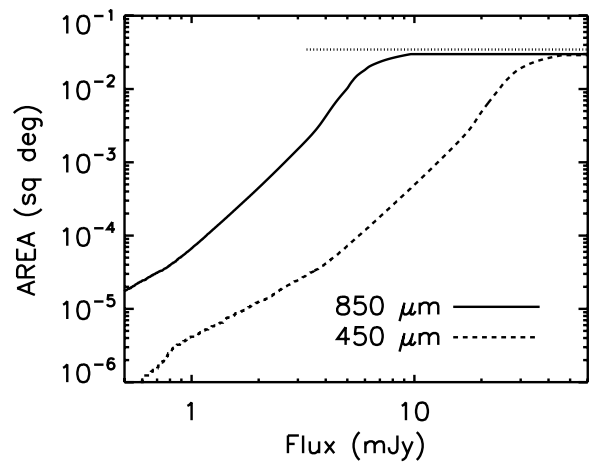


Figure 5. At $z = 2.5$, the source plane areas over which a source with a given flux in the source plane would be detected at $>4\sigma$ in the image plane. Dashed (solid) curves are for 450 (850) μm . For comparison, we also show the 850 μm image plane area as the horizontal dotted segment with the lower flux limit representing four times the 850 μm rms at the center of the image.

In a blank-field survey, the differential number counts can simply be calculated by dividing each source in a given flux bin by the area surveyed, summing these measurements, and then dividing by the flux bin width. However, in massive cluster fields, because of the gravitational lensing, the area used to divide each source is not simply the image plane area. It should be the total source plane area in which each source is located and could be significantly detected with its flux.

To find the detectable source plane area for each source, we gridded the image plane into $1''$ pixels and projected it back to the source plane at the source redshift. The total image plane area is the sum of any part of the map that has more than one-ninth of the central exposure time (Table 2). We found the spatial boundary of the source plane and then calculated the total source plane area. The average magnification of our observations at a given redshift is the ratio between the image plane area and the source plane area, which is 1.16 at both wavelengths at $z = 2.5$. We then regridded the source plane back into $1''$ pixels and projected them to the image plane. We counted the number of source grid points that were detectable at $>4\sigma$ on the image plane, assuming that each source grid emits the specified flux, and then multiplied the total number of points by 1 arcsec^2 to obtain the total detectable source plane area. In Figure 5, we demonstrate the source plane areas over which a source with a given flux in the source plane could be detected at $>4.0\sigma$ in the image plane, assuming $z = 2.5$.

We inverted the source plane area of each individual source to obtain the source surface density. Then, we added up the surface density of sources lying within each flux bin and divided that sum by the flux bin width to obtain the differential counts. The differential counts are best described by a broken power law, because once the map is sensitive enough to resolve the bulk of the EBL, the faint-end slope of the counts needs to be shallower than the bright-end slope so that the total EBL is finite. We performed χ^2 fits using the broken power law with basically two different slopes on each side of the characteristic flux. The sources with the characteristic flux dominate the contribution to the EBL. The broken power law is of the form

$$\frac{dN}{dS} = \begin{cases} N_0 \left(\frac{S}{S_0}\right)^{-\alpha} & \text{if } S \leq S_0 \\ N_0 \left(\frac{S}{S_0}\right)^{-\beta} & \text{if } S > S_0 \end{cases} \quad (3)$$

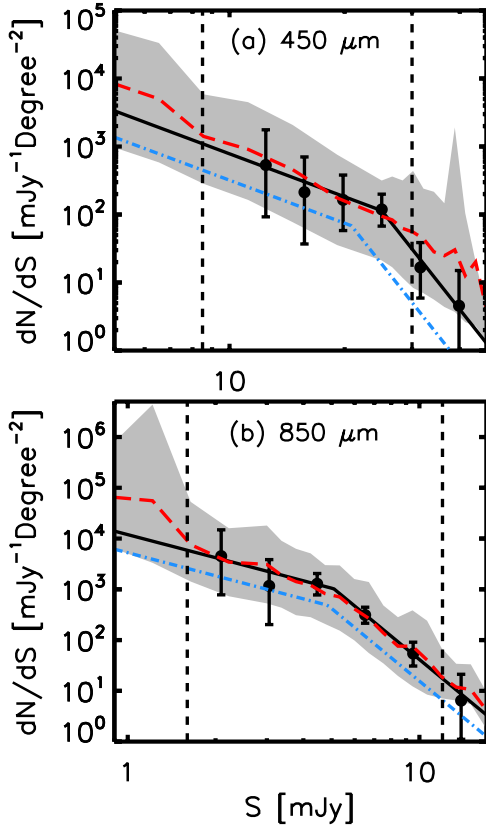


Figure 6. Raw and simulated differential number counts at (a) $450 \mu\text{m}$ and (b) $850 \mu\text{m}$. In each panel, the black circles are the raw number counts, and the black curves are the χ^2 broken power law fits to the raw number counts. The red dashed curves, representing the true number counts, are the final adopted model curves for our Monte Carlo simulations (see Section 4.2). The blue dot-dashed curves and the shaded regions are, respectively, the recovered mean number counts and the 90% confidence range obtained from the Monte Carlo simulations. The flux ranges enclosed by the black dashed lines are where the recovered curves are well constrained.

(A color version of this figure is available in the online journal.)

Table 8
 χ^2 Fits on the 450 and $850 \mu\text{m}$ Raw Differential Number Counts

Wavelengths	Equation	N_0	S_0	α	β
450	(3)	114	25.0	2.10	7.12
850	(3)	1024	5.09	1.51	4.75

We show the results of our fits in Table 8. We also plot them in Figure 6 (black lines), along with the raw number counts (black circles). Given the complicated effects of gravitational lensing, uneven sensitivity, and confusion, the true number counts and the errors on the raw number counts are best estimated with Monte Carlo simulations.

4.2. Simulations

We first estimated the true noise using the Jackknife resampling technique by subtracting two maps that were each created from co-adding roughly half of the data. Since the real sources, regardless of the significance of the detection, are subtracted off, the residual maps are source-free real noise maps. We then estimated the true noise from the noise maps scaled by a factor of $\sqrt{t_1 \times t_2 / (t_1 + t_2)}$, with t_1 and t_2 representing the exposure time of each pixel from the two maps. We found central noise values of 3.82 and $0.72 \text{ mJy beam}^{-1}$ at $450 \mu\text{m}$ and $850 \mu\text{m}$, re-

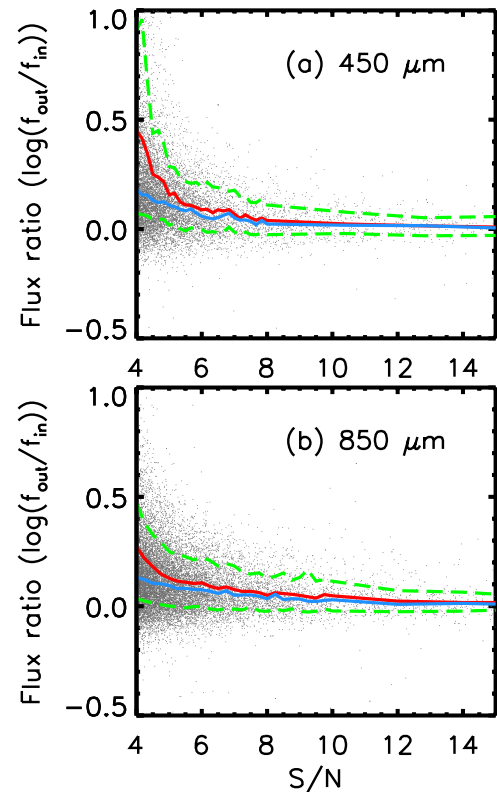


Figure 7. Ratio between the delensed fluxes of the detected sources and the input fluxes from our Monte Carlo simulations. The black dots are $\sim 10,000$ simulated data points. The red (blue) curves are the mean (median) value of the flux ratio in the different S/N bins. The area enclosed by the green dashed curves represents the 1σ range relative to the mean values.

(A color version of this figure is available in the online journal.)

spectively, about $0.1 \text{ mJy beam}^{-1}$ lower than the original maps containing faint sources.

We then took the broken power law fits from Section 4.1 as the underlying models of the source populations, drew sources from these models, and populated them onto the source plane at $z = 2.5$ at random positions with no clustering. For bright sources, where the average number of input sources is less than one, we randomized their input as either one or zero, with the number of each being determined by the probability of seeing a source at that flux. We imaged the sources back onto the image plane using LENSTOOL, added them into the true noise maps, and then ran through the same procedure of source extraction and number counts calculation that we performed on the data. Note that because DIMM performs a high-pass filtering in Fourier space to filter out the low spatial frequency structures, our data maps are not sensitive to the zeroth-order scaling factor seen in our simulated maps due to many evenly distributed faint sources. We therefore applied the filter on the simulated maps before we proceeded to extract sources.

We iterated this procedure 500 times using at least 10,000 simulated data points each time and compared the recovered curves from the simulations that connected the mean values of each flux bin with the models. We found a systematic flux/count boost, which we investigated by tracing the input source properties of each detection. For each $>4\sigma$ source in the output maps, we identified the brightest input source located within the beam area as the counterpart and plotted its flux ratio in Figure 7. We did not remove potential false detections if the ratio were unreasonably high (i.e., a flux ratio >2), since we kept every

Table 9
The True Number Counts Curves at 450 and 850 μm
from the Monte Carlo Simulations

Wavelengths	Equation	N_0	S_0	α	β
450	(3)	68.4	20.8	2.10	7.12
850	(3)	485	4.85	1.51	4.75

detected source for the real counts, and it is critical to follow the same procedure for the simulated counts as for the real counts. At $S/N = 4$, we found median flux boosting factors of 1.61 and 1.31 at 450 μm and 850 μm , respectively. At 850 μm , this is in agreement with previous SCUBA studies. Cowie et al. (2002) performed a Monte Carlo simulation with a single slope input model of the A370 field and found the boosting factor to be around 1.25 at 850 μm . Various SCUBA blank-field studies also found similar results (Eales et al. 2000; Scott et al. 2002; Wang et al. 2004).

We then applied the corrections to the models by adjusting the positions of the characteristic fluxes and the scaling factors of the broken power laws. Note that we kept the measured slopes, since the boost is much more sensitive to the S/N than to the intrinsic fluxes.

We list the parameters of our final adopted model curves (hereafter referred to as our true number counts curves) in Table 9, and we plot them in Figure 6 (blue dot-dashed curves). We show the recovered mean number counts as the red dashed curves. We use gray shading to represent the 90% confidence region. Between ~ 1.6 –12 mJy at 850 μm and ~ 8.5 –30 mJy at 450 μm (black dashed vertical lines), the recovered mean number counts curves agree well with the broken power law fits to the data (black solid curves) and are well constrained with at least 100 data points per bin. The fainter-end counts are overestimated by the curves at both wavelengths. Because they are not well sampled due to the small source plane area, the output counts are dominated by serendipitous detections from strongly lensed sources, and the number counts curves based on them are highly boosted. The same argument can be applied to the brighter-end counts, where the curves are more unstable and scattered. The surface density of bright sources is too low to generate an adequate number of sources given the survey area of our observations. Thus, the output counts curves are dominated by the boosted fainter sources.

Because our maps have not yet reached the confusion limit, the cause of the boost is mostly due to the statistical fluctuations of the source flux measurements for flux-limited observations, known as the Eddington bias (Eddington 1913). Previous SCUBA studies (e.g., Eales et al. 2000) also found that the dominant boosting factor is the noise.

4.3. True Number Counts and the EBL

We took our $>4\sigma$ sources and deboosted their fluxes based on the mean flux boosting ratio shown in Figure 7 (red curves). We computed the true number counts in a similar way as presented in Section 4.1. However, instead of using the delensed fluxes, we added up the surface densities of sources with delensed and deboosted fluxes lying within each flux bin. Tables 10 and 11 give the true differential number counts and the number of sources in each flux bin at 450 μm and 850 μm . The errors are based on Poisson statistics (Gehrels 1986). The faintest fluxes we detected after delensing and deboosting are ~ 1.1 mJy at 850 μm and ~ 4.5 mJy at 450 μm .

Table 10
450 μm True Number Counts

S_{450} (mJy)	N	dN/dS^a ($\text{mJy}^{-1} \text{deg}^{-2}$)	S_{450} (mJy)	$N(>S)^b$ (deg^{-2})
5.54	2	$1455^{+1919}_{-939.7}$	4.50	5786^{+7632}_{-3738}
8.09	3	$367.5^{+357.5}_{-200.1}$	6.58	2765^{+2690}_{-1505}
11.83	2	$83.14^{+109.7}_{-53.71}$	9.61	1650^{+2176}_{-1066}
17.29	3	$161.2^{+156.8}_{-87.76}$	14.05	$1281^{+1246}_{-697.3}$
25.26	1	$19.43^{+44.69}_{-16.07}$	20.53	$236.2^{+543.2}_{-195.3}$
36.92	1	$3.76^{+8.65}_{-3.11}$	30.00	$52.09^{+119.8}_{-43.08}$

Table 11
850 μm True Number Counts

S_{850} (mJy)	N	dN/dS^a ($\text{mJy}^{-1} \text{deg}^{-2}$)	S_{850} (mJy)	$N(>S)^b$ (deg^{-2})
1.39	1	6176^{+14205}_{-5108}	1.10	7683^{+17670}_{-6353}
2.13	2	$553.0^{+729.4}_{-357.2}$	1.69	4064^{+5361}_{-2626}
3.27	8	$1835^{+905.8}_{-634.8}$	2.58	3568^{+1762}_{-1235}
5.01	7	$361.7^{+194.8}_{-133.4}$	3.96	$1044^{+562.1}_{-384.8}$
7.68	5	$76.44^{+51.71}_{-33.02}$	6.07	$281.1^{+190.1}_{-121.4}$
11.78	1	$6.88^{+15.81}_{-5.69}$	9.30	$34.05^{+78.33}_{-28.16}$

Notes.

^a Differential number counts.

^b Cumulative number counts.

We plot our true 450 μm differential number counts (black squares) and true number counts curves from our Monte Carlo simulations (black curves) in Figure 8(a), along with the results from *Herschel* (Oliver et al. 2010) at 350 μm and 500 μm (olive and pink squares, respectively). In Figure 8(b), we plot our true 850 μm differential number counts (black circles) and true number counts curves from our Monte Carlo simulations (black curves), along with the results of previous SCUBA 850 μm lensing cluster surveys given in Knudsen et al. (2008) (purple filled circles) and of the SHADES SCUBA blank-field survey (Coppin et al. 2006; blue filled circles). We also show the Knudsen et al. (2008) 850 μm fit to their data (blue curve). In Figures 8(c) and (d), we plot the cumulative number counts at 450 μm and 850 μm , respectively, which we calculated by summing all the source densities above a given flux.

At 450 μm , our bright-end number counts agree with the faint-end counts from *Herschel* (Figure 8); however, our observations probe a factor of ~ 4 deeper. Above ~ 30 mJy, our curves slightly underestimate the *Herschel* counts, but our survey area is not large enough to make this result significant. Because of the steeply rising counts as we probe to fainter source fluxes, our 450 μm source surface density increases by more than a factor of 10 compared with the results from *Herschel*.

With our 450 μm true number counts curve, the amount of 450 μm EBL we directly resolve is ~ 66.4 Jy deg^{-2} above 4.5 mJy. This is $\sim 47\%$ – 61% of the total 450 μm EBL, depending on the adopted model (Puget et al. 1996; Fixsen et al. 1998). We expect to resolve 100% of the 450 μm EBL at ~ 1 mJy based on our counts model, although we note that since our model curve does not converge, the curve must turn over to a shallower slope in the fainter flux regime. Recently, the closest measurements to our results are from the deep 500 μm surveys using *Herschel*. Again, the confusion limit caused by *Herschel*'s small aperture size (large beam size) hampers its capability to

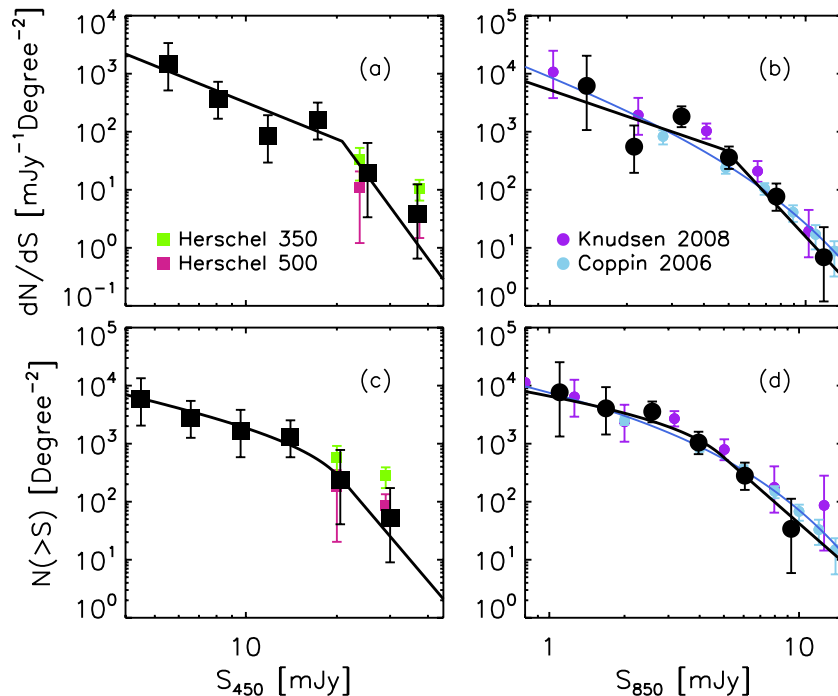


Figure 8. SCUBA-2 A370 differential number counts at (a) 450 μm and (b) 850 μm and cumulative number counts at (c) 450 μm and (d) 850 μm . The black filled symbols (squares for 450 μm and circles for 850 μm) are the deboosted and deboosted number counts given in Tables 10 and 11. In all panels, the black curves are our true number counts curves (i.e., the blue dot-dashed curves from Figure 6). The number counts obtained from *Herschel* at 350 μm and 500 μm (Oliver et al. 2010) are denoted by olive and pink squares, respectively, in panels (a) and (c). Blue curves in (b) and (d) show the 850 μm fit from Knudsen et al. (2008). Their number counts are denoted by purple filled circles. The blank-field counts from SHADES (Coppin et al. 2006) are denoted by blue filled circles. (A color version of this figure is available in the online journal.)

resolve the EBL (6%), and the direct counts from *Herschel* are a factor of ~ 4 shallower than the present observations (Figure 8).

A $P(D)$ analysis using pixel flux distributions was used to probe deeper in the *Herschel* maps; however, the results were not well constrained at the fainter end beyond the characteristic flux (Glenn et al. 2010). Béthermin et al. (2012) performed a stacking analysis on a deep *Herschel* 500 μm map using a sample of 24 μm sources. They found that they were able to resolve 55% of the EBL down to 2 mJy. However, a stacking analysis can only provide information on the selected sample as a whole and does not reveal the true flux distribution of the individual sources. Our observations directly resolve the contributing sources, clearly reveal the characteristic flux, and provide an unbiased sample of sources for further study.

Moreover, we estimate that without lensing, the deboosted counts can be probed to ~ 8 mJy at 450 μm , corresponding to $\sim 30\%$ – 40% of the 450 EBL. An extremely deep SCUBA-2 450 μm blank-field observation can resolve $\sim 70\%$ – 90% of the EBL before hitting the confusion limit (estimated at ~ 2 mJy given the source density reaching 1 per 30 beam area) based on our current counts model. However, based on the current sensitivity of SCUBA-2, taking into account flux boosting, to directly detect sources with 2 mJy 450 μm intrinsic fluxes at 4 sigma, one needs more than 100 hr of observing time, which is not practical. Thus, to fully resolve 450 μm EBL using SCUBA-2, we will need to observe the lensing fields.

At 850 μm , our number counts agree nicely with previous SCUBA results in both blank-field and cluster lensed surveys. Based on our true number counts curve, our observations are able to resolve directly $\sim 40\%$ – 57% of the 850 μm EBL above 1.1 mJy with the range again corresponding to the uncertainty in the EBL determination. Our 850 μm observations are not as sensitive as many of the confusion-limited blank-field SCUBA

surveys; however, thanks to the gravitational lensing, we are able to resolve more EBL than what has been reported from the blank-field SCUBA surveys above 2 mJy (20%–30%; e.g., Barger et al. 1999a).

5. 450-850-RADIO COMPARISON

The tight, universal correlation between FIR and radio luminosity among normal galaxies in the local universe (Helou et al. 1985; Condon 1992) has been used to find the counterparts to the 850 μm SMGs and to estimate their redshifts (e.g., Carilli & Yun 1999; Barger et al. 2000). However, this method has not been tested on 450 μm selected sources. With our newly detected 450 μm sources and the deep 20 cm map ($1\sigma \sim 5.7 \mu\text{Jy}$) of the A370 field (Wold et al. 2012), we are ideally equipped to conduct such a study. Here we study the properties of our submillimeter samples in terms of the source matches, the positional uncertainties, and the redshift distribution estimated through the various flux ratios.

Note that the differential number counts are computed by dividing the summed source surface densities within a flux bin by the flux bin width, which means that the boosting effect on the number counts comes from the mean flux boosting factors (red curves in Figure 7). This is shown in Section 4.3 where we used the mean flux boosting factors to deboost the raw number counts and to compute the true number counts shown in Figure 8 that agrees with the underlying true number counts models.

However, to deboost the fluxes of individual sources for characteristic analysis, the median flux ratios (blue curves in Figure 7) are more representative for the majority of the population because of the non-Gaussian distribution caused by fake sources with extreme output-to-input flux ratios, especially at lower S/N ($S/N < 6$; Figure 7). The median flux ratios can

be significantly different than the mean flux ratios, a factor of ~ 2.7 versus ~ 1.6 at 4σ at $450\ \mu\text{m}$. Thus, for the rest of this paper, when we refer to the intrinsic submillimeter fluxes for individual sources, they are delensed and deboosted, where the latter has been done using the median flux boosting factors at the source S/N.

5.1. Source Matches

Due to the negative K -correction at $850\ \mu\text{m}$ and the positive K -correction at $20\ \text{cm}$ (Carilli & Yun 1999; Barger et al. 2000; Blain et al. 2002), $850\ \mu\text{m}$ SMGs with radio counterparts are biased against high-redshift sources, and only a fraction of the $850\ \mu\text{m}$ SMGs are seen in the radio. It has been found that around 60% of the $850\ \mu\text{m}$ SMGs with fluxes $>4\ \text{mJy}$ have radio counterparts in radio images with a 1σ sensitivity of $\sim 6\ \mu\text{Jy}$ (Barger et al. 2000; Wang et al. 2004; Ivison et al. 2007; Biggs et al. 2011). However, because of the FIR–radio correlation, as the radio images reach deeper, there should be a higher fraction of SMGs that have radio counterparts. Indeed, the latest study by Barger et al. (2012) show that very deep $20\ \text{cm}$ interferometric observations with a 1σ sensitivity of $\sim 2.5\ \mu\text{Jy}$ can find all SMGs with $850\ \mu\text{m}$ fluxes above $3\ \text{mJy}$.

We cross-identified our submillimeter catalogs with the $>5\sigma$ radio catalog of Wold et al. (2012), created from a $20\ \text{cm}$ survey of A370 with a 1σ sensitivity of $\sim 6\ \mu\text{Jy}$. We found that 8 out of 18 (44%) of the $850\ \mu\text{m}$ sources with intrinsic fluxes $>4\ \text{mJy}$ have robust radio counterparts within the $850\ \mu\text{m}$ beam at the $>5\sigma$ level.

We may reduce our radio S/N threshold if we have more accurate submillimeter positions. We ran a simulation to estimate the probability of a randomly positioned $450\ \mu\text{m}$ beam selecting a $>3\sigma$ random noise fluctuation on a simulated normal-distributed radio map. We found the probability to be $\sim 5\%$. The probability should be even lower if there are counterparts at other wavelengths (e.g., $850\ \mu\text{m}$). Note that Biggs et al. (2011) considered radio sources with 5% of the so-called corrected Poissonian probability (Browne & Cohen 1978) to be secure counterparts for SMGs. Using the $450\ \mu\text{m}$ data, we identified four more $>3\sigma$ radio counterparts to the $850\ \mu\text{m}$ sources. Thus, in total, 12/18 or 66.7% of the $850\ \mu\text{m}$ sources with intrinsic fluxes $>4\ \text{mJy}$ have radio matches, which is consistent with what has been reported in the literature.

For the $450\ \mu\text{m}$ sources, the fraction having secure ($>3\sigma$) radio counterparts is 85% (17/20). This high match rate could mean that both the $450\ \mu\text{m}$ sources with intrinsic fluxes $>6\ \text{mJy}$ and the $20\ \text{cm}$ emission are preferentially tracing lower redshift starbursting galaxies, because both have positive K -corrections at high redshifts. Meanwhile, 67% (8/12) of the $>4\sigma$ $450\ \mu\text{m}$ sources are detected at $850\ \mu\text{m}$, while the recovery rate for $>4\sigma$ $850\ \mu\text{m}$ sources at $450\ \mu\text{m}$ is slightly lower (13/24; 54%).

The moderate match between $450\ \mu\text{m}$ and $850\ \mu\text{m}$ sample again implies that the SMG population is diverse and different selection methods reveal only parts of the overall population. For example, SMGs detected only at $450\ \mu\text{m}$ tend to have a higher dust temperature and/or lower redshift (Casey et al. 2012), whereas the $850\ \mu\text{m}$ sources without radio or $450\ \mu\text{m}$ counterparts provide the most probable candidate high-redshift sources (e.g., Riechers et al. 2010; Walter et al. 2012).

5.2. Positional Uncertainties

In the absence of $450\ \mu\text{m}$ observations or submillimeter or millimeter interferometry, radio sources have been widely used

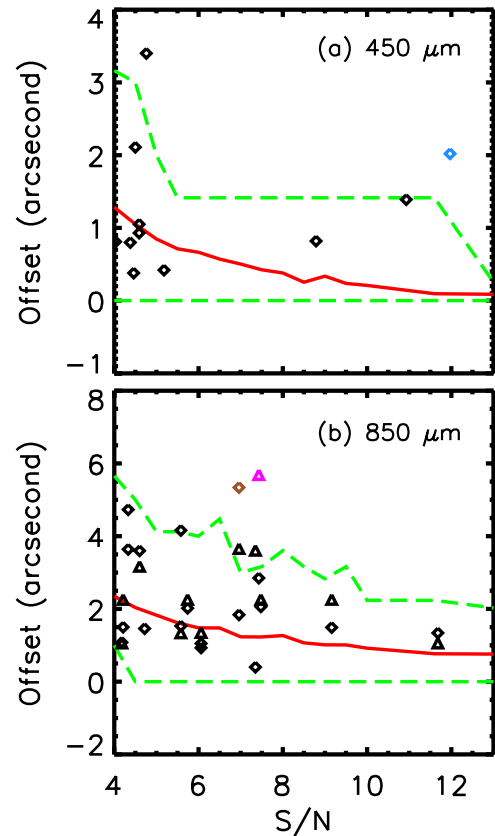


Figure 9. Positional offsets between the output and the brightest input sources within the beam area from our Monte Carlo simulations (red curves). The areas enclosed by the green dashed curves represent the 90% confidence ranges relative to the mean values. The diamonds are the offsets between our cataloged (a) $450\ \mu\text{m}$ sources and (b) $850\ \mu\text{m}$ sources relative to the 5σ radio sources. The triangles in (b) are the offsets between the $450\ \mu\text{m}$ and $850\ \mu\text{m}$ sources. A370-450.1/A370-850.1, A370-450.18/A370-850.7 and A370-450.9/A370-450.11/A370-850.5 are plotted with the blue diamond in (a), the brown diamond and the magenta triangle in (b), respectively.

(A color version of this figure is available in the online journal.)

to locate counterparts to the SMGs detected at $850\ \mu\text{m}$ by single-dish telescopes (e.g., Barger et al. 2000; Smail et al. 2002; Chapman et al. 2005; Pope et al. 2005). This method has been shown to be appropriate for many of the sources using high-resolution submillimeter interferometric observations, though in some cases there may be multiple counterparts rather than a single source (Younger et al. 2007, 2009; Wang et al. 2011; Barger et al. 2012; Karim et al. 2012). In contrast to following up each source individually with interferometers, we can statistically examine the method by comparing the positional offsets between radio and submillimeter sources from real observations and the offsets obtained from Monte Carlo simulations. In theory, if the radio emission traces the submillimeter emission, then the observational results should agree statistically with the simulations.

The details of the simulations are described in Section 4.2. We note that in the simulations, at both wavelengths we treated the brightest input source as the counterpart, and we gridded the maps to $1'' \times 1''$ in order to match with the real submillimeter data maps. We plot our results in Figure 9 at (a) $450\ \mu\text{m}$ and (b) $850\ \mu\text{m}$. The observational offsets between the submillimeter sources and their secure radio counterpart candidates are in diamonds in both panels, and the simulated mean offsets are denoted by red curves with the 90% confidence range enclosed

by green dashed curves. The observational results generally agree with our simulations, except for two sources, A370-450.1/A370-850.1 (blue diamond in Figure 9(a)) and A370-450.18/A370-850.7 (brown diamond in Figure 9(b)). A detailed analysis of these two sources is given in the later sections and the [Appendix](#), in which we conclude that those two sources are likely to be complex systems with multiple sources contributing emission at different wavelengths. Taking A370-450.1/A370-850.1 as an example, recent studies of this source have revealed its complex nature, including multiple sources having different characteristics being located within $1''$ – $2''$ of one another (more details are given on this source in the [Appendix](#)) and evidence for a significant offset between the dust and radio emission (Genzel et al. 2003; Ivison et al. 2010). Our statistical diagnosis serves as a simple test as to whether there is a common origin for the emission seen in the different wavebands.

We also plot the offsets between the $450\ \mu\text{m}$ and $850\ \mu\text{m}$ sources on Figure 9(b) (black triangles). Again, we find good statistical agreement between the observational offsets and the offsets that we obtain from the simulations, which supports the idea that the $450\ \mu\text{m}$ sources are a good positional tracer for the $850\ \mu\text{m}$ sources. Although the $450\ \mu\text{m}$ positions are less accurate than the radio positions, the $450\ \mu\text{m}$ emission has the advantage of directly tracing the thermal dust emission, just as the $850\ \mu\text{m}$ emission does.

Similar to the situation for A370-450.1 mentioned above, there is a complex system in the submillimeter, A370-450.9/A370-450.11/A370-850.5, that lies off the simulated curve in Figure 9(b) (magenta triangle). This could be another example of a multiple, where different sources contribute emission at different wavelengths, and sources selected at different wavelengths may have different origins (Wang et al. 2011; Barger et al. 2012). Note that in this plot we show the offset between A370-450.11 and A370-850.5. The offset between A370-450.9 and A370-850.5 is even larger.

In general, there is a slight upward bias for the real data relative to the simulated mean curve, which could be caused by the fact that some of the counterparts may not be correct. As we show in subsequent sections, some of the sources have multiple radio counterparts within the beam area, which is an indication of a complex nature. Including incorrect counterparts leads to a large dispersion and, in our case, an upward bias.

5.3. Millimetric Redshifts

We estimated the redshifts of each source using the $850\ \mu\text{m}$ -to- $450\ \mu\text{m}$ and submillimeter-to- $20\ \text{cm}$ flux ratios assuming a modified blackbody SED template with $\beta = 1$ (dust emissivity) and $T_d = 47\ \text{K}$ (dust temperature) from the local starbursting galaxy Arp 220 (Klaas et al. 1997; Barger et al. 2000). In Table 12, we show the redshifts of each individual source estimated using three different flux ratios. We show dots when there is not a measurement for both fluxes (e.g., $z_{450/\text{radio}}$ on A370-850.11) or when there are multiple counterpart candidates (e.g., A370-450.17/850.4 with its multiple radio counterparts). In many cases, the redshift estimates using different flux ratios, in particular, $850\ \mu\text{m}$ -to- $450\ \mu\text{m}$ and $850\ \mu\text{m}$ -to- $20\ \text{cm}$, agree with one other to within the uncertainties. A noticeable disagreement is seen for SMGs not detected at $850\ \mu\text{m}$ (e.g., A370-450.6, 450.8, 450.10, 450.12). Here the flux ratios between $850\ \mu\text{m}$ and $450\ \mu\text{m}$ indicate a low redshift, while the flux ratios between $450\ \mu\text{m}$ and $20\ \text{cm}$ indicate higher redshifts. Given that $450\ \mu\text{m}$ data suffer from a positive K -correction, much as $20\ \text{cm}$ data do, such sources are more

Table 12
Redshifts

ID ₄₅₀	ID ₈₅₀	$z_{850/450}$	$z_{450/\text{radio}}$	$z_{850/\text{radio}}$	z_{adopted}^a
A370-450.1	A370-850.1	2.800
A370-450.2	A370-850.3	$0.00^{+0.76}_{-0.00}$	$0.97^{+0.07}_{-0.07}$	$0.84^{+0.07}_{-0.07}$	1.060
A370-450.3	A370-850.2	$2.08^{+0.81}_{-0.84}$	$1.85^{+0.19}_{-0.18}$	$1.90^{+0.13}_{-0.12}$	$1.90^{+0.13}_{-0.12}$
A370-450.4	A370-850.18	$0.00^{+1.73}_{-0.00}$	$1.43^{+0.22}_{-0.22}$	$1.18^{+0.18}_{-0.20}$	1.519
A370-450.5	A370-850.6	$3.48^{+1.30}_{-1.31}$	$5.95^{+0.00}_{-2.30}$	$4.47^{+1.15}_{-0.76}$	$4.47^{+1.15}_{-0.76}$
A370-450.6	...	<0.01	$5.95^{+0.00}_{-0.98}$...	(0.01)
A370-450.7	A370-850.8	$2.52^{+1.50}_{-1.61}$	$2.52^{+1.50}_{-1.61}$
A370-450.8	...	<0.80	$1.74^{+0.36}_{-0.33}$...	(0.80)
A370-450.9	A370-850.5
A370-450.10	...	<0.94	$3.08^{+1.48}_{-0.79}$...	(0.94)
A370-450.11	A370-850.5
A370-450.12	...	<1.80	$3.67^{+2.28}_{-1.13}$...	(1.80)
A370-450.13	A370-850.26	$0.66^{+2.47}_{-0.66}$	>5.95	>3.22	...
A370-450.14	A370-850.17	$1.52^{+2.07}_{-1.52}$	$2.99^{+1.55}_{-0.83}$	$2.53^{+0.58}_{-0.49}$	$2.53^{+0.58}_{-0.49}$
A370-450.15	A370-850.9	$3.31^{+1.68}_{-1.70}$	$1.95^{+0.48}_{-0.43}$	$2.29^{+0.31}_{-0.30}$	$2.29^{+0.31}_{-0.30}$
A370-450.16	A370-850.10	$3.63^{+1.70}_{-1.70}$	$3.63^{+1.70}_{-1.70}$
A370-450.17	A370-850.4	$4.61^{+1.60}_{-1.45}$	$4.61^{+1.60}_{-1.45}$
A370-450.18	A370-850.7	$5.01^{+1.71}_{-1.52}$	$5.01^{+1.71}_{-1.52}$
A370-450.19	A370-850.25	$2.28^{+2.28}_{-2.28}$	$1.42^{+0.34}_{-0.35}$	$1.58^{+0.25}_{-0.27}$	$1.58^{+0.25}_{-0.27}$
A370-450.20	A370-850.15	$2.80^{+2.18}_{-2.38}$	$3.04^{+1.87}_{-0.94}$	$3.08^{+0.65}_{-0.55}$	$3.08^{+0.65}_{-0.55}$
...	A370-850.11	>2.93	...	>4.29	(4.29)
...	A370-850.12	>2.14	...	>4.25	(4.25)
...	A370-850.13	>1.98	...	>4.71	(4.71)
...	A370-850.14	>1.99	...	$2.34^{+0.39}_{-0.37}$	$2.34^{+0.39}_{-0.37}$
...	A370-850.16	>1.78
...	A370-850.19	>0.81	...	>4.12	(4.12)
...	A370-850.20	>0.00	...	>4.49	(4.49)
...	A370-850.21	>1.50	...	>4.12	(4.12)
...	A370-850.22	>1.31	...	>3.61	(3.61)
...	A370-850.23	>1.23	...	$3.08^{+0.79}_{-0.63}$	$3.08^{+0.79}_{-0.63}$
...	A370-850.24	>0.48	...	>3.41	(3.41)

Notes.

^a Values with three digits after the decimal point are spectroscopic redshifts.

likely to be at low redshifts. The fact they have abnormally high $450\ \mu\text{m}$ fluxes probably indicates that they have higher dust temperatures than what we assumed in the SED template. Thus, the $850\ \mu\text{m}$ fluxes lie below the detection limit.

In the final column of Table 12, we give our adopted redshift for each source that had good constraints on the redshift estimation. Redshifts with three digits after the decimal point represent the spectroscopic measurements. We primarily adopted the redshifts estimated through the $850\ \mu\text{m}$ -to- $20\ \text{cm}$ flux ratio, since it has recently been shown to be a reasonable redshift estimator with good accuracies (Barger et al. 2012). We adopted the redshifts estimated from the $850\ \mu\text{m}$ -to- $450\ \mu\text{m}$ flux ratio whenever the $850\ \mu\text{m}$ -to- $20\ \text{cm}$ flux ratio was unavailable.

We plot histograms of our redshifts in Figure 10. Sources detected at both $450\ \mu\text{m}$ and $850\ \mu\text{m}$ (green shading) have a median redshift of $z \sim 2.5$. The redshift distribution of the sources detected only at $450\ \mu\text{m}$ (red shading) is denoted by blue (red) lines. We adopted the upper limits of the redshifts estimated using the $850\ \mu\text{m}$ -to- $450\ \mu\text{m}$ flux ratio for the sources detected only at $450\ \mu\text{m}$. For $850\ \mu\text{m}$ sources without good redshift constraints, we adopted the lower limits estimated using the

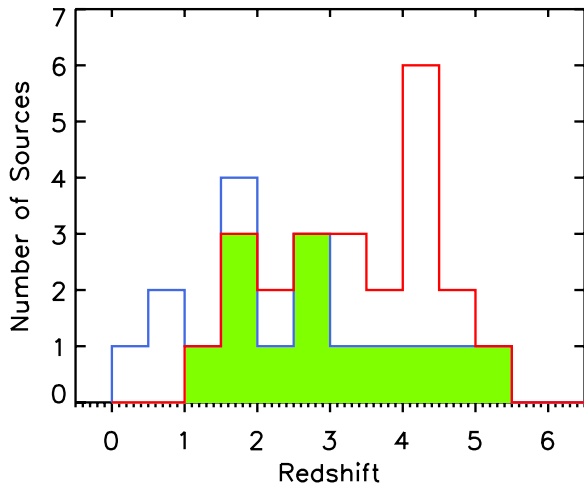


Figure 10. Histograms of the source redshifts from Table 12. The redshift distribution for the sources detected at both $450\ \mu\text{m}$ and $850\ \mu\text{m}$ (green shading) has a median $z \sim 2.5$. The red histogram outlines the redshift distribution for the $850\ \mu\text{m}$ sources only, while the blue histogram outlines the redshift distribution for the $450\ \mu\text{m}$ sources only. The median redshift for all the $450\ \mu\text{m}$ (850 μm) sources is $z \sim 2.3$ ($z \sim 3.4$). A370-450.13 is not included in this plot, since in this case the redshifts estimated from the different flux ratios diverge.

(A color version of this figure is available in the online journal.)

$850\ \mu\text{m}$ -to-20 cm flux ratios. In the final column of Table 12, we show these redshift limits with parenthesis. All the $850\ \mu\text{m}$ sources have a median redshift of $z \sim 3.4$, while all the $450\ \mu\text{m}$ sources have a median redshift of $z \sim 2.3$. These results generally agree with the picture that $450\ \mu\text{m}$ sources preferentially trace lower redshift dusty sources, while $850\ \mu\text{m}$ sources tend toward higher redshifts. We do, however, caution that because there are many issues about fitting the FIR SED template for SMGs, such as the degeneracy between source redshift, dust temperature, and dust emissivity (Casey 2012), our results are first-order estimations and should be used carefully.

6. COUNTERPART IDENTIFICATIONS AND DISCUSSION

In this section, we restrict our sample to the 14 sources that are detected at $>5\sigma$ in at least one submillimeter waveband for their robust detections and better constraints on the astrometry (Section 5.2). We refer to these 14 sources as our SCUBA-2 robust sample. We note that the most part of our $450\ \mu\text{m}$ map has a sensitivity lower than the *Herschel* confusion limit ($1\sigma \sim 6.8\ \text{mJy}$; Nguyen et al. 2010) at similar wavelengths, and even at 5σ level, majority (10 out of 14) of our SCUBA-2 robust sample would not be found by *Herschel* at 4σ .

Except for the *Spitzer* and *Chandra* data, the data at other wavelengths fully cover the SCUBA-2 surveyed area. We show the schematic *Spitzer* and *Chandra* coverage in Figure 11, where the $450\ \mu\text{m}$ and $850\ \mu\text{m}$ sources in the SCUBA-2 robust sample are marked with red and blue symbols, and the identification numbers of the $850\ \mu\text{m}$ sources are given. The *Spitzer* coverage at various wavelengths is denoted by the green lines, while the gray area shows the area observed by *Chandra*.

In Figure 12, we give postage stamp images for each of the 14 sources, including an inverse gray-scale z -band image, a false color J , H , K_s image, an inverse gray-scale $4.5\ \mu\text{m}$ image, and an inverse gray-scale 20 cm image. We use cyan and red circles to represent the positional error of the $450\ \mu\text{m}$ and $850\ \mu\text{m}$ sources with 95% confidence.

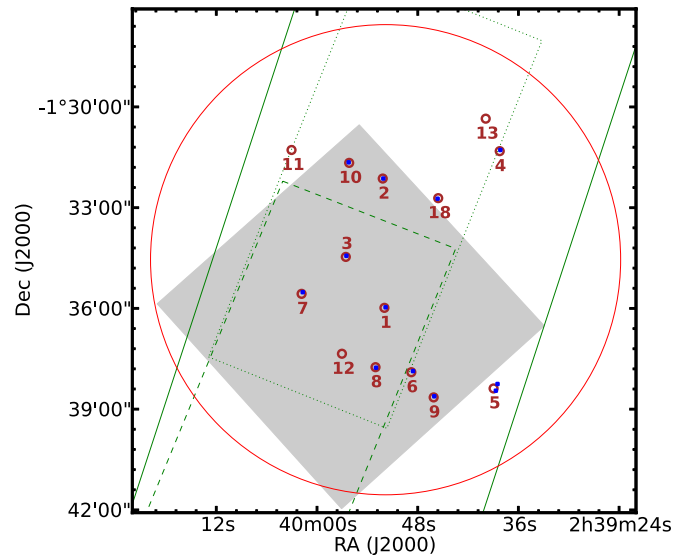


Figure 11. Schematic sky coverage of the A370 field. The approximate SCUBA-2 coverage is denoted by the red circle with a radius of $7'$. The *Spitzer* $3.6\ \mu\text{m}$ and $4.5\ \mu\text{m}$ coverage is marked with the green solid lines, and the $5.8\ \mu\text{m}$ and $8.0\ \mu\text{m}$ coverages are marked, respectively, with the green dashed and dotted lines. The blue dots (red circles) represent the locations of our $450\ \mu\text{m}$ ($850\ \mu\text{m}$) sources in our SCUBA-2 robust sample. The numbers given are the identifications of the $850\ \mu\text{m}$ sources. The gray area shows the X-ray coverage obtained by *Chandra*.

(A color version of this figure is available in the online journal.)

In Table 13, we give the delensed photometry of each candidate counterpart from the NIR to the radio. We label these candidate counterparts with the submillimeter source identification followed by a small “a,” “b,” or “c,” if there are multiple candidates. We use dots in the table when the submillimeter source lies outside the coverage of a particular wavelength image. We discuss the individual sources in the Appendix. Note that because there are no sources in our SCUBA-2 robust sample that are only detected at $450\ \mu\text{m}$, when referring to individual sources hereafter, we will use the $450\ \mu\text{m}$ identifications for sources detected at both $450\ \mu\text{m}$ and $850\ \mu\text{m}$, and we will use the $850\ \mu\text{m}$ identifications for sources only detected at $850\ \mu\text{m}$.

6.1. X-Ray Candidate Counterparts

While a number of studies have shown that most of the FIR luminosity from SMGs comes from star formation, the issue of what fraction of SMGs contain an AGN is far from settled. Results have ranged from as many as 75% (Alexander et al. 2005; radio-detected SMGs) down to $\sim 10\%$ – 30% (Georgantopoulos et al. 2011; *Spitzer*-detected SMGs). Existing *Chandra* observations of the A370 field partially cover our SCUBA-2 survey area and include nine $850\ \mu\text{m}$ sources and eight $450\ \mu\text{m}$ sources from the SCUBA-2 robust sample. We cross-correlated the source catalogs in Barger et al. (2001) and found two counterparts in hard X-rays (A370-450.1, A370-450.2) and one in soft X-rays (A370-450.16). This gives a fraction of $3/9$ robust $850\ \mu\text{m}$ sources containing an AGN ($\sim 33\%$), which is similar to what Georgantopoulos et al. (2011) found but much lower than the results of Alexander et al. (2005). Note that both of these studies from the literature used much deeper X-ray maps with exposure times of 1 Ms and 2 Ms, respectively. Thus, it is not surprising that we find a lower fraction of submillimeter sources containing an AGN. For our robust $450\ \mu\text{m}$ sources, the fraction is $3/8$ ($\sim 38\%$).

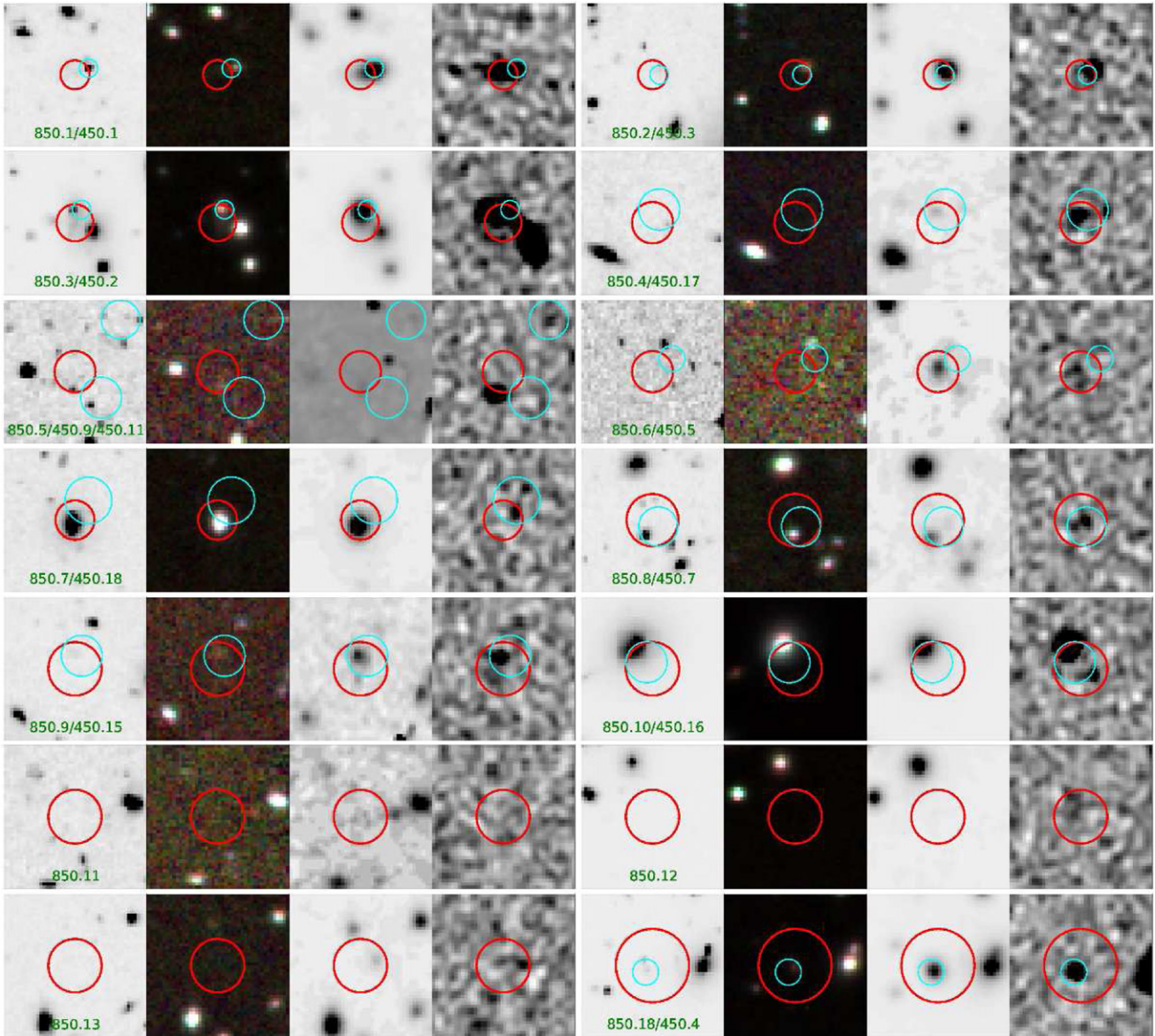


Figure 12. Postage stamp images of the 5σ submillimeter sources in our SCUBA-2 robust sample. The images from left to right in each panel are an inverse gray-scale z -band image, a false color near-infrared (J, H, K) image, an inverse gray-scale $4.5 \mu\text{m}$ image, and an inverse gray-scale 20 cm image. The images are plotted with a dynamical range from 1% to 99% using a linear scale. The angular size of each image is $22'' \times 22''$. The cyan and red circles represent, respectively, the positional uncertainties with 95% confidence at $850 \mu\text{m}$ and $450 \mu\text{m}$ (see Section 5.1).

(A color version of this figure is available in the online journal.)

6.2. IR Candidate Counterparts

The IR properties of the $850 \mu\text{m}$ SMGs have been extensively studied from the NIR to *Spitzer* $3.6 \mu\text{m}$ to $24 \mu\text{m}$ (Frayser et al. 2003, 2004; Clements et al. 2004; Pope et al. 2005; Hainline et al. 2009; Wang et al. 2012). One of the goals of studying the IR properties of the SMGs is to seek color criteria that could efficiently select the correct counterparts to the $850 \mu\text{m}$ SMGs, especially given their large positional uncertainties.

While the NIR color spans a wide range, and there is not yet a single selection method that is successful in choosing the SMGs, an MIR color selection proposed by Yun et al. (2008) using the $8.0 \mu\text{m}/4.5 \mu\text{m}$ versus $5.8 \mu\text{m}/3.6 \mu\text{m}$ flux ratio diagram seems to be able to separate SMGs from other field galaxies. It has been argued that this MIR color selection is too general in that it includes more than 50% of the field galaxies in the GOODS-N field (Hainline et al. 2009). However, it is still a

good first-order test on our candidate counterparts. We plot any available candidate counterparts from Table 13 that have all four *Spitzer* passband measurements in Figure 13(a). The enclosed area denoted by the solid lines represents the color space of the MIR color selection. We plot the normal field galaxies selected from a deep K_s survey of the GOODS-N field as small gray dots (Wang et al. 2010). For visual reference, the MIR measurements on the SMGs observed with the SMA are plotted as triangles for the GOODS-N sample (Barger et al. 2012) and asterisks for the AzTEC/COSMOS sample (Younger et al. 2007, 2009). Most of our counterpart candidates, except A370-450.7a and 450.18a, are located within the SMG color regions; thus, A370-450.7a and A370-450.18a could be false counterparts based on this selection.

Another interesting way of selecting SMGs in IR color space is to use the $K_s-4.5 \mu\text{m}$ color (KIEROS; Wang et al. 2010, 2012). As opposed to the sources selected by the traditional red

Table 13
NIR, MIR, and Radio Photometry

Source ID	R.A. ^a (J2000.0)	Decl. ^a (J2000.0)	Offset ^b (")	<i>J</i> (mag)	<i>H</i> (mag)	<i>K_s</i> (mag)	3.6 μ m (mag)	4.5 μ m (mag)	5.8 μ m (mag)	8.0 μ m (mag)	20 cm (μ Jy)	<i>z</i>
850.1/450.1	2 39 52.0	-1 35 58.5	2.0	21.8	21.4	21.2	20.4	20.0	19.4	18.9	164.5	2.8000
850.2/450.3	2 39 52.1	-1 32 07.2	0.8	21.8	21.0	20.2	19.2	18.9	...	19.1	150.4	...
850.3/450.2	2 39 56.6	-1 34 26.6	1.3	19.9	19.7	19.2	18.4	18.4	18.3	18.3	245.5	1.0600
850.4/450.17a	2 39 38.3	-1 31 17.4	2.1	>23.5	>23.0	>23.0	22.8	22.1	61.7	...
850.4/450.17b	2 39 38.0	-1 31 16.6	2.4	>23.5	>23.0	>23.0	23.4	22.7	25.8	...
850.5/450.11a	2 39 39.0	-1 38 25.8	2.9	23.2	22.6	21.9	...	22.0	275.0	3.8219
850.5/450.11b	2 39 38.8	-1 38 28.1	2.0	23.0	>23.0	>23.0	>23.3	>23.3	>23.0	>22.6	<16.7	...
850.5/450.9	2 39 38.5	-1 38 14.6	0.4	>23.5	>23.0	>23.0	...	22.4	18.4	...
850.6/450.5	2 39 48.8	-1 37 53.6	3.9	>23.6	>23.1	>23.1	21.9	21.3	18.3	...
850.7/450.18a	2 40 01.8	-1 35 34.8	4.0	18.9	18.8	18.6	19.2	19.4	19.7	20.2	<14.4	...
850.7/450.18b	2 40 01.7	-1 35 33.2	2.2	>23.7	>23.2	>23.2	>23.5	>23.2	>23.2	>22.8	23.3	...
850.7/450.18c	2 40 01.6	-1 35 29.7	2.0	>23.7	>23.2	>23.2	>23.5	>23.2	>23.2	>22.8	17.9	...
850.8/450.7a	2 39 53.1	-1 37 47.5	2.5	20.2	20.3	20.1	20.7	20.9	20.9	22.1	<14.8	...
850.8/450.7b	2 39 52.9	-1 37 45.3	1.3	>23.7	>23.2	>23.2	22.5 ^c	21.5 ^c	22.3 ^c	21.4 ^c	23.8	...
850.8/450.7c	2 39 53.0	-1 37 45.9	0.5	>23.7	>23.2	>23.2	22.5 ^c	21.5 ^c	22.3 ^c	21.4 ^c	15.2	...
850.9/450.15	2 39 46.1	-1 38 37.0	1.1	23.3	22.2	22.2	21.2	20.6	67.6	...
850.10/450.16a	2 39 56.3	-1 31 36.7	2.5	16.0	16.1	16.3	16.4	16.6	...	14.3	938.1	0.0286
850.10/450.16b	2 39 56.1	-1 31 41.1	2.9	>23.7	>23.2	>23.2	>23.5	>23.2	...	>22.8	50.0	...
850.13	2 39 39.8	-1 30 20.2	1.7	>23.5	>23.0	>23.0	22.6	21.7	...	21.2	23.1	...
850.18/450.4	2 39 45.6	-1 32 43.6	0.6	20.9	20.7	20.2	19.5	19.2	...	18.9	144.3	1.5190

Notes.

^a Positions are extracted from the radio counterpart, if present, and otherwise from the optical counterpart. For sources without any radio or optical counterparts, we used the positions from the images with the best resolution.

^b Offsets are calculated with the 450 μ m position as the reference, except for 850.13.

^c Source blended.

color criteria, such as distant red galaxies (DRGs; Franx et al. 2003) and extremely red objects (EROs; Elston et al. 1988; Hu & Ridgway 1994), KIEROs with $K_s-4.5 \mu\text{m}$ (AB) > 1.6 are mostly dusty starbursting galaxies, and one-third of the SMGs that have submillimeter interferometric follow-up are KIEROs (Wang et al. 2012). We examine our counterpart candidates on a $K_s-4.5 \mu\text{m}$ versus $3.6 \mu\text{m}-4.5 \mu\text{m}$ diagram in Figure 13(b). This is similar to Figure 1 of Wang et al. (2012). We again plot the normal field galaxies selected from a deep K_s survey of the GOODS-N field as small gray dots as in Figure 13(a). The SMGs in the GOODS-N field with robust counterpart identifications from Barger et al. (2012) are plotted as triangles, and our candidate counterparts are plotted as filled circles. Most of the SMGs cluster at the top-right corner, indicating a very red nature. Three of our candidate counterparts, including A370-450.7a and A370-450.18a, are located below the SMG locus in $K_s-4.5 \mu\text{m}$ color, which could mean that either they are simply not the true SMG counterparts or that they are located at lower redshifts (e.g., A370-450.16a is at $z = 0.0286$). While the $K_s-4.5 \mu\text{m}$ color is an indicator for redshifts (Wang et al. 2012), the fact that most of our candidates are located below the KIEROs color cut is evidence that sources detected at both 450 μm and 850 μm are likely at lower redshifts than sources selected purely at 850 μm , which is consistent with our previous results.

In Figure 14(a), we plot K_s versus the 850 $\mu\text{m}/20 \text{ cm}$ flux ratio using sources having unambiguous radio counterparts in our SCUBA-2 robust sample (filled circles) along with the secure GOODS-N SMG sample with SMA follow-up from Barger et al. (2012; triangles). We find a correlation between these two parameters using the non-parametric Spearman's rank correlation test ($\rho = 0.44$, 15 degree of freedom, P -value = 0.04), where the higher the submillimeter to radio flux fraction, the fainter the K_s magnitude. We derive a minimum χ^2 fit (black

curve) of $\log_{10}(f_{850\mu\text{m}}/f_{20\text{cm}}) = 0.23 \times K_s(\text{AB}) - 3.24$. We also plot K -band magnitude versus redshift in Figure 14(b) using any spectroscopic redshifts available for the sources in Figure 14(a) (including the GOODS-N sample) and millimetric redshifts (shown with error bars) for the ones without spectroscopic redshifts. While the majority of the sources have spectroscopic redshifts, the data distribution is very similar in both panels, indicating that the 850 $\mu\text{m}/20 \text{ cm}$ flux ratio is a good indicator of redshift. The correlation we found could mean that the bright SMG population has a similar rest-frame optical luminosity, and the observed K_s -band dimming is caused by the source distance. A similar correlation with K -band magnitude versus redshift for SCUBA sources was found by Clements et al. (2004) and Pope et al. (2005). Our correlation reasonably agrees with their results.

7. SUMMARY

In this paper, we present results from our SCUBA-2 450 μm and 850 μm observations of the massive lensing cluster field A370. Our observations reach a 1σ sensitivity of 3.92 mJy beam⁻¹ and 0.82 mJy beam⁻¹ at 450 μm and 850 μm , respectively. We summarize our findings below.

1. We detected in total 20 sources at 450 μm and 26 sources at 850 μm with a significance of $>4\sigma$. Using the latest lensing model for A370, we derived the intrinsic submillimeter fluxes and observed number counts. We ran Monte Carlo simulations to obtain the true number counts that take into account lensing effects, completeness, noise distributions, and flux boosting.
2. We found that our observations resolve $\sim 47\%$ – 61% of the 450 μm EBL above 4.5 mJy and $\sim 40\%$ – 57% of the 850 μm EBL above 1.1 mJy. The 450 μm counts are the deepest determination to date at this wavelength.

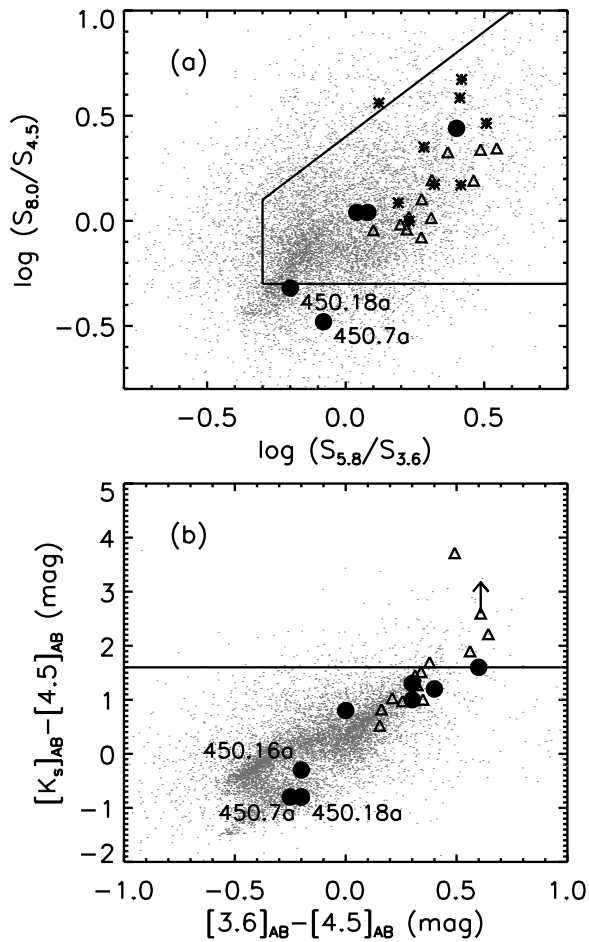


Figure 13. IR color-color diagram with filled circles representing our SCUBA-2 robust sample sources with measurements in all four passbands and triangles showing the GOODS-N SMG sample observed with the SMA by Barger et al. (2012). (a) $8.0 \mu\text{m}/4.5 \mu\text{m}$ vs. $5.8 \mu\text{m}/3.6 \mu\text{m}$ color-color diagram. Another SMG sample obtained with the AzTEC/COSMOS survey at $890 \mu\text{m}$ and observed with the SMA is denoted by asterisks (Younger et al. 2007, 2009). The area enclosed by the solid lines is the color space proposed by Yun et al. (2008) for selecting SMGs. (b) $K_s - 4.5 \mu\text{m}$ vs. $3.6 \mu\text{m} - 4.5 \mu\text{m}$ color-color diagram. The field galaxies selected in a deep K_s survey of the GOODS-N field by Wang et al. (2012) are plotted in gray dots, and the area above the horizontal line shows their KIEROs selection ($K_s - 4.5 \mu\text{m}$ (AB) > 1.6). Two sources (450.7 α and 450.18 α) have the same flux ratios, so we have moved the data point of 450.7 α 0.05 mag to the left for clarity.

3. We used a statistical method to examine the origin of the $450 \mu\text{m}$ and $850 \mu\text{m}$ emission by plotting the observational positional offsets between the $450 \mu\text{m}$ and $850 \mu\text{m}$ emission against the ideal distribution of offsets, assuming common origins, using our Monte Carlo simulations. We found statistically that the $450 \mu\text{m}$ emission is a good positional tracer for the $850 \mu\text{m}$ population.
4. We estimated the redshift distributions for our submillimeter samples using millimetric flux ratios assuming a modified blackbody SED template from the local starbursting galaxy Arp 220. We found a median redshift of ~ 2.5 for only the sources detected at both $450 \mu\text{m}$ and $850 \mu\text{m}$, $z \sim 2.3$ for all the $450 \mu\text{m}$ sources, and $z \sim 3.4$ for all the $850 \mu\text{m}$ sources.
5. The percentage of SMGs having secure radio counterparts is 85% for $450 \mu\text{m}$ sources with intrinsic fluxes $> 6 \text{ mJy}$ and $\sim 67\%$ for $850 \mu\text{m}$ sources with intrinsic fluxes $> 4 \text{ mJy}$. Of the $> 4\sigma$ $450 \mu\text{m}$ sources, 67% are detected in $850 \mu\text{m}$, while the recovery rate for $850 \mu\text{m}$ sources at $450 \mu\text{m}$ is

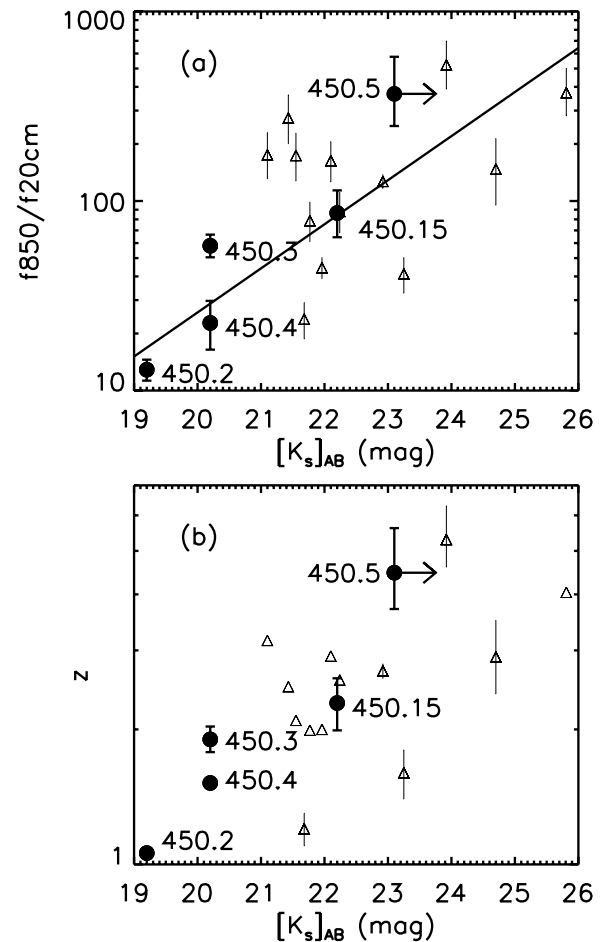


Figure 14. (a) $850 \mu\text{m}/20 \text{ cm} - K_s$ color-magnitude diagram. Our sample sources are shown in filled circles with their IDs. The linear solid curve represents the minimum χ square fit to our data points. Results from submillimeter interferometric follow-up on GOODS-N SMGs are plotted in triangles (Barger et al. 2012). (b) Redshift- K_s diagram using the same sample sources as described in (a). Millimetric redshifts are adopted with error bars whenever the spectroscopic redshifts are not available.

$\sim 54\%$. The recovered rate we found is consistent with the scenario that both $450 \mu\text{m}$ and 20 cm emission trace lower redshift dusty starbursting galaxies, while $850 \mu\text{m}$ emission comes from dusty sources located at higher redshifts.

6. We identified potential counterparts in various wavelengths from the X-ray to the MIR for our SCUBA-2 robust sample ($S/N > 5$). Three X-ray counterparts are found to be correlated with our robust submillimeter sample. The AGN fraction of our $450 \mu\text{m}$ sample is $3/8$, 38%, and it is $3/9$ (33%) for the $850 \mu\text{m}$ sample. The IR colors of our candidate counterparts mostly agree with the locations of SMGs in previous diagrams, except for a few sources that may be incorrectly identified. We found a correlation between the $850 \mu\text{m}/20 \text{ cm}$ flux ratio and the K_s band.

We gratefully acknowledge support from NSF grant AST 0709356 (C.-C.C., L.L.C.), the University of Wisconsin Research Committee with funds granted by the Wisconsin Alumni Research Foundation (A.J.B.), the David and Lucile Packard Foundation (A.J.B.), and the National Science Council of Taiwan grant 99-2112-M-001-012-MY3 (W.-H.W.). C.M.C. is generously supported by a Hubble Fellowship provided by Space Telescope Science Institute, grant HST-HF-51268.01-A.

We thank the referee for an insightful review, Tim Jenness, Per Friberg, David Berry, Douglas Scott, and Edward Chapin for helpful discussions on data reduction, JAC support astronomers Iain Coulson, Holy Thomas, and Antonio Chrysostomou, and JCMT telescope operators Jim Hoge, William Montgomerie, and Jan Wouterloot. The James Clerk Maxwell Telescope is operated by the Joint Astronomy Centre on behalf of the Science and Technology Facilities Council of the United Kingdom, The Netherlands Organisation for Scientific Research, and the National Research Council of Canada. Additional funds for the construction of SCUBA-2 were provided by the Canada Foundation for Innovation. We acknowledge the cultural significance that the summit of Mauna Kea has to the indigenous Hawaiian community.

APPENDIX INDIVIDUAL SOURCES

A370-850.1 (450.1). This is the brightest submillimeter source at both $450\ \mu\text{m}$ and $850\ \mu\text{m}$ in the A370 region and the first submillimeter source discovered by SCUBA (Smail et al. 1997). Follow-up observations with high spatial and spectral resolution have revealed its complex nature. Based on several optical and CO spectral line observations (Frayser et al. 1998; Ivison et al. 1998; Genzel et al. 2003), one of the two optical counterparts, L1, was first identified as the main submillimeter emitter, possibly due to its AGN and star-forming activity, while the nature of the other optical source, L2, was debated between scattered AGN light from L1 (Vernet & Cimatti 2001) or the remnant of a merger (Ivison et al. 1998). The most recent studies by Ivison et al. (2010) using the CO $J = 1 \rightarrow 0$ line and data newly obtained from *Hubble* and *Spitzer* argue that a heavily dust-obscured starburst between L1 and L2, L2SW, is more likely to be the true counterpart. They also argue that together with a bright UV emitter, L1N, this could be a merger system with at least two galaxies. However, due to the positional uncertainties of all the sources, it is hard to rule out the scenario proposed by Genzel et al. (2003) of a gas reservoir residing in a massive, extended disk around L1. Interestingly, our $450\ \mu\text{m}$ emission peaks on L1, while the $850\ \mu\text{m}$ emission peaks on L2SW. Based on our results, we argue that both L1 and L2SW contribute to the FIR emission. Future subarcsecond observations using the EVLA or ALMA will be the key to fully understanding a system with such complexity. For simplicity, in this paper we only provide the photometric information for L1.

A370-850.2 (450.3). With the help of better spatial resolution data at $450\ \mu\text{m}$, an optically faint, MIR, and radio bright counterpart is clearly identified. The redshift estimate for this source using the $850\ \mu\text{m}$ -to-20 cm flux ratio (see Section 5.3) is $\sim 1.90 \pm 0.12$.

A370-850.3 (450.2). This source was also detected in a SCUBA survey at both $450\ \mu\text{m}$ and $850\ \mu\text{m}$ (Smail et al. 2002). Two possible counterparts are detected across all bandpasses. Detailed observations with the Keck II LRIS spectrograph show that L3, an AGN at $z = 1.06$ with a ring morphology, is more likely to be the counterpart than L5, a passive cluster elliptical (Barger et al. 1999b). This was confirmed by high-resolution interferometric observations using the SMA (Chen et al. 2011), and our high S/N $450\ \mu\text{m}$ detection confirms this result.

A370-850.4 (450.17). Both a 5σ and a 4σ radio source are located within the submillimeter positional errors. Both sources

are optically and IR faint and therefore very dusty. It is likely that both radio sources contribute part of the submillimeter emission.

A370-850.5 (450.9/450.11). The submillimeter morphology of A370-850.5 extends toward A370-450.9. We subtracted the PSF centered at the peak position of A370-850.5 to obtain the $850\ \mu\text{m}$ flux for A370-450.9, which is 3.91 ± 1.49 mJy. A 3σ radio source sits close to the A370-450.9 position with faint emission at $4.5\ \mu\text{m}$. A bright radio source candidate counterpart (A370-450.11a) with a spectroscopic redshift of $z = 3.8219$ is located on the verge of the 95% confidence positional area. Another candidate counterpart (A370-450.11b) is a faint z -band source. This region is the most complex system in our survey with potentially up to three sources (A370-450.9, A370-450.11, and A370-850.5) contributing to the submillimeter emission.

A370-850.6 (450.5). One *Spitzer* source is located within the submillimeter positional error. It has a 3σ radio counterpart and is not visible in the optical and NIR. From the $850\ \mu\text{m}$ -to-20 cm flux ratio, we estimated a redshift of $z \sim 4.47$ for this source.

A370-850.7 (450.18). A bright galaxy candidate counterpart (A370-450.18a) is located very close to the $850\ \mu\text{m}$ position. This galaxy was reported in earlier optical and NIR cluster survey work (Stanford et al. 1995; Margoniner & de Carvalho 2000). We estimated the redshift of the SMG to be $z \sim 5$ from the $850\ \mu\text{m}$ -to- $450\ \mu\text{m}$ flux ratio. Although there is no redshift measurement for this source, the fact that it is resolved in the optical and IR makes it likely to be at low redshifts. In addition, the fact that the SED of A370-450.18a decays toward longer wavelengths makes it unlikely to be the origin of the submillimeter emission. More tentative candidate counterparts are selected within the $450\ \mu\text{m}$ positional error, where there are two $>3.5\sigma$ optically faint, IR faint, radio detections. If those two radio sources are proven to be the correct counterparts, then they would be great examples of how $450\ \mu\text{m}$ positions can be used to select counterparts to $850\ \mu\text{m}$ sources.

A370-850.8 (450.7). The candidate counterpart A370-450.7a is seen in the optical and IR and was detected in other optical (g, r, i) surveys (Margoniner & de Carvalho 2000). Faint emission in the *Spitzer* passbands can be seen toward the two faint radio source candidate counterparts, A370-450.7b and A370-450.7c. We estimated a redshift of $z \sim 2.5$ for the SMG using the $850\ \mu\text{m}$ -to- $450\ \mu\text{m}$ flux ratio.

A370-850.9 (450.15). One optically faint but MIR and radio bright counterpart is identified. We estimated a redshift of $\sim 2.29 \pm 0.3$ for this source using the $850\ \mu\text{m}$ -to-20 cm flux ratio.

A370-850.10 (450.16). A bright local galaxy candidate counterpart (A370-450.16a) with $z = 0.0286$ is seen in the northeast. This source was reported in various observations from the optical to the X-ray (Margoniner & de Carvalho 2000; Barger et al. 2001; Metcalfe et al. 2003). Although its IR color does not put it around the locus of a typical SMG, we cannot rule out the possibility of A370-450.16a contributing to the submillimeter emission, since it is bright in the radio. Meanwhile, another radio source candidate counterpart (A370-450.16b) is located in the southwest. Its optical and IR faint nature makes it another plausible counterpart. It is likely that both A370-450.16a and A370-450.16b contribute part of the submillimeter emission.

A370-850.18 (450.4). An optically faint, MIR and radio bright counterpart is clearly identified by the $450\ \mu\text{m}$ emission. This source has a redshift of $z = 1.519$ (Wold et al. 2012), which agrees within the errors with our redshift estimations for this source using the flux ratios.

REFERENCES

- Alexander, D. M., Bauer, F. E., Chapman, S. C., et al. 2005, *ApJ*, **632**, 736
- Barger, A. J., Cowie, L. L., Bautz, M. W., et al. 2001, *AJ*, **122**, 2177
- Barger, A. J., Cowie, L. L., & Richards, E. A. 2000, *AJ*, **119**, 2092
- Barger, A. J., Cowie, L. L., & Sanders, D. B. 1999a, *ApJL*, **518**, 5
- Barger, A. J., Cowie, L. L., Sanders, D. B., et al. 1998, *Natur*, **394**, 248
- Barger, A. J., Cowie, L. L., Smail, I., et al. 1999b, *AJ*, **117**, 2656
- Barger, A. J., Wang, W.-H., Cowie, L. L., et al. 2012, *ApJ*, **761**, 89
- Bautz, M. W., Malm, M. R., Baganoff, F. K., et al. 2000, *ApJL*, **543**, 119
- Bertin, E., & Arnouts, S. 1996, *A&AS*, **117**, 393
- B  thermin, M., Le Floch, E., Ibert, O., et al. 2012, *A&A*, **542**, A58
- Biggs, A. D., Ivison, R. J., Ibar, E., et al. 2011, *MNRAS*, **413**, 2314
- Blain, A. W., Chapman, S. C., Smail, I., & Ivison, R. 2004, *ApJ*, **611**, 52
- Blain, A. W., Kneib, J.-P., Ivison, R. J., & Smail, I. 1999, *ApJL*, **512**, 87
- Blain, A. W., Smail, I., Ivison, R. J., Kneib, J.-P., & Frayer, D. T. 2002, *PhR*, **369**, 111
- Browne, I. W. A., & Cohen, A. M. 1978, *MNRAS*, **182**, 181
- Carilli, C. L., & Yun, M. S. 1999, *ApJL*, **513**, 13
- Casey, C. M. 2012, *MNRAS*, **425**, 3094
- Casey, C. M., Chapman, S. C., Beswick, R. J., et al. 2009, *MNRAS*, **399**, 121
- Casey, C. M., Berta, S., B  thermin, M., et al. 2012, *ApJ*, **761**, 139
- Chapman, S. C., Blain, A. W., Smail, I., & Ivison, R. J. 2005, *ApJ*, **622**, 772
- Chapman, S. C., Scott, D., Borys, C., & Fahlman, G. G. 2002, *MNRAS*, **330**, 92
- Chapman, S. C., Smail, I., Blain, A. W., & Ivison, R. J. 2004, *ApJ*, **614**, 671
- Chen, C.-C., Cowie, L. L., Wang, W.-H., Barger, A. J., & Williams, J. P. 2011, *ApJ*, **733**, 64
- Clements, D., Eales, S., Wojciechowski, K., et al. 2004, *MNRAS*, **351**, 447
- Condon, J. J. 1974, *ApJ*, **188**, 279
- Condon, J. J. 1992, *ARA&A*, **30**, 575
- Coppin, K., Chapin, E. L., Mortier, A. M. J., et al. 2006, *MNRAS*, **372**, 1621
- Cowie, L. L., Barger, A. J., & Kneib, J.-P. 2002, *AJ*, **123**, 2197
- Dempsey, J. T., Holland, W. S., Chrysostomou, A., et al. 2012, *Proc. SPIE*, **8452**, 845202
- Dole, H., Lagache, G., Puget, J.-L., et al. 2006, *A&A*, **451**, 417
- Eales, S., Lilly, S., Gear, W., et al. 1999, *ApJ*, **515**, 518
- Eales, S., Lilly, S., Webb, T., et al. 2000, *AJ*, **120**, 2244
- Eddington, A. S. 1913, *MNRAS*, **73**, 359
- Elston, R., Rieke, G. H., & Rieke, M. J. 1988, *ApJL*, **331**, 77
- Fazio, G. G., Hora, J. L., Allen, L. E., et al. 2004, *ApJS*, **154**, 10
- Fixsen, D. J., Dwek, E., Mather, J. C., Bennett, C. L., & Shafer, R. A. 1998, *ApJ*, **508**, 123
- Franx, M., Labb  , I., Rudnick, G., et al. 2003, *ApJL*, **587**, 79
- Frayer, D. T., Armus, L., Scoville, N. Z., et al. 2003, *AJ*, **126**, 73
- Frayer, D. T., Ivison, R. J., Scoville, N. Z., et al. 1998, *ApJL*, **506**, 7
- Frayer, D. T., Reddy, N. A., Armus, L., et al. 2004, *AJ*, **127**, 728
- Gehrels, N. 1986, *ApJ*, **303**, 336
- Genzel, R., Baker, A. J., Tacconi, L. J., et al. 2003, *ApJ*, **584**, 633
- Georgantopoulos, I., Rovilos, E., & Comastri, A. 2011, *A&A*, **526**, A46
- Glenn, J., Conley, A., B  thermin, M., et al. 2010, *MNRAS*, **409**, 109
- Hainline, L. J., Blain, A. W., Smail, I., et al. 2009, *ApJ*, **699**, 1610
- Helou, G., Soifer, B. T., & Rowan-Robinson, M. 1985, *ApJL*, **298**, 7
- Ho, P. T. P., Moran, J. M., & Lo, K. Y. 2004, *ApJL*, **616**, 1
- Hogg, D. W. 2001, *AJ*, **121**, 1207
- Holland, W., MacIntosh, M., Fairley, A., et al. 2006, *Proc. SPIE*, **6275**, 62751E
- Holland, W. S., Robson, E. I., Gear, W. K., et al. 1999, *MNRAS*, **303**, 659
- Hu, E. M., Cowie, L. L., Barger, A. J., et al. 2010, *ApJ*, **725**, 394
- Hu, E. M., & Ridgway, S. E. 1994, *AJ*, **107**, 1303
- Hughes, D. H., Serjeant, S., Dunlop, J., et al. 1998, *Natur*, **394**, 241
- Ivison, R. J., Greve, T. R., Dunlop, J. S., et al. 2007, *MNRAS*, **380**, 199
- Ivison, R. J., Smail, I., Le Borgne, J.-F., et al. 1998, *MNRAS*, **298**, 583
- Ivison, R. J., Smail, I., Papadopoulos, P. P., et al. 2010, *MNRAS*, **404**, 198
- Jenness, T., Berry, D., Chapin, E., et al. 2011, in ASP Conf. Ser. 442, *Astronomical Data Analysis Software and Systems XX*, ed. I. N. Evans, A. Accomazzi, D. J. Mink, & A. H. Rots (San Francisco, CA: ASP), **281**
- Jenness, T., Cavanagh, B., Economou, F., & Berry, D. S. 2008, in ASP Conf. Ser. 394, *Astronomical Data Analysis Software and Systems XVII*, ed. R. W. Argyle, P. S. Bunclark, & J. R. Lewis (San Francisco, CA: ASP), **565**
- Karim, A., Swinbank, M., Hodge, J., et al. 2012, arXiv:1210.0249
- Keenan, R. C., Trouille, L., Barger, A. J., Cowie, L. L., & Wang, W.-H. 2010, *ApJS*, **186**, 94
- Klaas, U., Haas, M., Heinrichsen, I., & Schulz, B. 1997, *A&A*, **325**, L21
- Kneib, J., Ellis, R. S., Smail, I., Couch, W. J., & Sharples, R. M. 1996, *ApJ*, **471**, 643
- Knudsen, K. K., Kneib, J.-P., Richard, J., Petitpas, G., & Egami, E. 2010, *ApJ*, **709**, 210
- Knudsen, K. K., van der Werf, P.-P., & Kneib, J. P. 2008, *MNRAS*, **384**, 1611
- Larson, D., Dunkley, J., Hinshaw, G., et al. 2011, *ApJS*, **192**, 16
- Margoniner, V. E., & de Carvalho, R. R. 2000, *AJ*, **119**, 1562
- Metcalfe, L., Kneib, J.-P., McBreen, B., et al. 2003, *A&A*, **407**, 791
- Nguyen, H. T., Schulz, B., Levenson, L., et al. 2010, *A&A*, **518**, L5
- Oliver, S. J., Wang, L., Smith, A. J., et al. 2010, *A&A*, **518**, L21
- Pilbratt, G. L., Riedinger, J. R., Passvogel, T., et al. 2010, *A&A*, **518**, L1
- Pope, A., Borys, C., Scott, D., et al. 2005, *MNRAS*, **358**, 149
- Pope, A., Scott, D., Dickinson, M., et al. 2006, *MNRAS*, **370**, 1185
- Puget, J., Abergel, A., Bernard, J.-P., et al. 1996, *A&A*, **308**, L5
- Richard, J., Kneib, J.-P., Limousin, M., Edge, A., & Jullo, E. 2010, *MNRAS*, **402**, L44
- Riechers, D. A., Capak, P. L., Carilli, C. L., et al. 2010, *ApJL*, **720**, 131
- Scheuer, P. A. G. 1957, *Proc. Camb. Phil. Soc.*, **53**, 764
- Scott, S. E., Fox, M. J., Dunlop, J. S., et al. 2002, *MNRAS*, **331**, 817
- Serjeant, S., Dunlop, J. S., Mann, R. G., et al. 2003, *MNRAS*, **344**, 887
- Siringo, G., Kreysa, E., Kov  cs, A., et al. 2009, *A&A*, **497**, 945
- Smail, I., Ivison, R. J., Blain, A. W., et al. 1997, *ApJL*, **490**, 5
- Smail, I., Ivison, R. J., Blain, A. W., & Kneib, J.-P. 2002, *MNRAS*, **331**, 495
- Smol  i  , V., Navarrete, F., Aravena, M., et al. 2012, *ApJS*, **200**, 10
- Stanford, S. A., Eisenhardt, P. R. M., & Dickinson, M. 1995, *ApJ*, **450**, 512
- Vernet, J., & Cimatti, A. 2001, *A&A*, **380**, 409
- Walter, F., Decarli, R., Carilli, C., et al. 2012, *Natur*, **486**, 233
- Wang, W., Cowie, L. L., & Barger, A. J. 2004, *ApJ*, **613**, 655
- Wang, W., Cowie, L. L., Barger, A. J., & Williams, J. P. 2011, *ApJL*, **726**, 18
- Wang, W.-H., Barger, A. J., & Cowie, L. L. 2012, *ApJ*, **744**, 155
- Wang, W.-H., Cowie, L. L., Barger, A. J., Keenan, R. C., & Ting, H.-C. 2010, *ApJS*, **187**, 251
- Wardlow, J. L., Smail, I., Coppin, K. E. K., et al. 2011, *MNRAS*, **415**, 1479
- We  , A., Kov  cs, A., Coppin, K., et al. 2009, *ApJ*, **707**, 1201
- Werner, M. W., Roellig, T. L., Low, F. J., et al. 2004, *ApJS*, **154**, 1
- Wold, I. G. B., Owen, F. N., Wang, W.-H., Barger, A. J., & Keenan, R. C. 2012, *ApJS*, **202**, 2
- Younger, J. D., Fazio, G. G., Huang, J.-S., et al. 2007, *ApJ*, **671**, 1531
- Younger, J. D., Fazio, G. G., Huang, J. S., et al. 2009, *ApJ*, **704**, 803
- Yun, M. S., Aretxaga, I., Ashby, M. L. N., et al. 2008, *MNRAS*, **389**, 333